

1 Disparate energy consumption despite similar 2 network activity

3 Michael Deistler^{1,2}, Jakob H. Macke^{1,2,3*}, Pedro J. Gonçalves^{1,4*}

4 ¹Machine Learning in Science, Excellence Cluster 'Machine Learning', Tübingen University, Tübingen,
5 Germany; ²Computational Neuroengineering, Department of Electrical and Computer Engineering,
6 Technical University of Munich, Germany; ³Max Planck Institute for Intelligent Systems, Tübingen,
7 Germany; ⁴Center of Advanced European Studies and Research (caesar), Bonn, Germany

9 Abstract

10 Neural circuits can produce similar activity patterns from vastly different combinations of channel and synaptic con-
11 ductances. These conductances are tuned for specific activity patterns but might also reflect additional constraints,
12 such as metabolic cost or robustness to perturbations. How do such constraints influence the range of permissible
13 conductances? Here, we investigate how metabolic cost affects the parameters of neural circuits with similar activity
14 in a model of the pyloric network of the crab *Cancer borealis*. We use a novel machine learning method to identify a
15 range of network models that can generate activity patterns matching experimental data. We find that neural circuits
16 can consume largely different amounts of energy despite similar circuit activity. We then study how circuit param-
17 eters get constrained by minimizing energy consumption and identify circuit parameters that might be subject to
18 metabolic tuning. Finally, we investigate the interaction between metabolic cost and temperature robustness. We
19 show that metabolic cost can vary across temperatures, but that robustness to temperature changes does not nec-
20 essarily incur an increased metabolic cost. Our analyses show that, despite metabolic efficiency and temperature
21 robustness constraining circuit parameters, neural systems can generate functional, efficient, and robust network
22 activity with widely disparate sets of conductances.

24 Introduction

25 Neural activity arises from the interplay of mechanisms at multiple levels, including single-neuron and network mecha-
26 nisms. Several experimental and theoretical studies have found that neural systems can produce similar activity from
27 vastly different membrane and synaptic conductances [1–5], a property sometimes referred to as parameter degen-
28 eracy [6, 7]. Such parameter degeneracy has been argued to be a prerequisite for natural selection [6] and translates
29 into potential mechanisms of compensation for perturbations of the systems' parameters [3, 5, 8–13]. However, in
30 addition to a specific target activity, neural systems are likely subject to additional constraints such as the require-
31 ment to be energy efficient [14–16]. In order to understand experimentally observed variability and probe potential
32 compensation mechanisms in functioning neural systems, it is thus crucial to characterise the extent of the systems'
33 parameter degeneracy under such additional constraints.

34 Neuronal activity accounts for the majority of the energy consumed by the brain [17–19]. Energy is stored in
35 the ionic gradients across the cell membrane, and consumed mostly by action potentials and synaptic mechanisms.
36 Maintaining the ionic gradients requires the action of ion pumps, which consume ATP [14, 20]. Previous work has in-
37 vestigated the metabolic efficiency in small neural systems, often at the single neuron level and with few ion channels

*These authors contributed equally to this work

For correspondence: michael.deistler@uni-tuebingen.de; pedro.goncalves@uni-tuebingen.de

38 (often sodium, potassium, and leak) [14, 21, 22]. In these studies, it has been demonstrated that energy consump-
39 tion of single neurons can be reduced by tuning maximal conductances or time constants of gating variables, while
40 maintaining electrophysiological characteristics, e.g. spike width. However, questions regarding energy efficiency of
41 neural systems remain: First, it is unclear how previous findings in models with only sodium, potassium, and leak
42 currents extrapolate to the context of complex patterns of neuronal activity such as burst firing, which arise through
43 the interaction of a larger diversity of currents. Second, synaptic currents interact with single neuron properties
44 [11, 20, 23], raising the question of how membrane and synaptic conductances should be tuned in order to achieve
45 low metabolic cost. Third, energy efficiency has often been characterised for parts of, rather than the whole neural
46 system within which it operates. For example, the energy efficiency of single neurons is often studied in isolation of
47 the neural network it is immersed in [24–26], which precludes the full characterisation of how the operation of neural
48 systems impacts energy efficiency. Lastly, metabolic cost is only one of many constraints under which neural circuits
49 operate, and it is often unknown whether energy efficiency trades-off with other constraints (for a study of how en-
50 ergy efficiency trades off with temperature robustness in a single neuron model of the grasshopper, see Roemschied
51 et al. [27]).

52 Here, we investigate the energy efficiency of the pyloric network in the stomatogastric ganglion (STG) of the crab
53 *Cancer borealis* [28, 29], a canonical example of a neural system with parameter degeneracy [5]. The pyloric network
54 produces a triphasic motor pattern, and consists of a pacemaker kernel (anterior burster neuron, AB, and two pyloric
55 dilator neurons, PD), as well as two types of follower neurons (a single lateral pyloric, LP, and several pyloric, PY,
56 neurons), interconnected by inhibitory synapses. A model of this circuit with three model neurons (AB/PD, LP, PY),
57 each with eight membrane currents, and seven inhibitory synapses (Fig. 1a, details in Methods) has been shown to
58 be capable of producing similar network activity with widely different parameters [5].

59 We start by characterising the parameter degeneracy of this model: We apply a recently introduced machine learn-
60 ing tool for simulation-based inference, Sequential Neural Posterior Estimation (SNPE) [13] to estimate the full set of
61 membrane and synaptic conductances for which the model reproduces experimental data. We reduce the number of
62 model simulations required to run SNPE by introducing an additional classifier which detects and rejects parameter-
63 combinations that produce non-bursting model outputs [30]. After characterising the parameter degeneracy in the
64 model, we show that disparate circuit configurations can have different energy consumption despite similar activity.
65 Notably, a reduced but significant parameter degeneracy is present in the model even when enforcing circuits to have
66 *both* similar activity and energy consumption. Furthermore, energy consumption is linearly predictable from circuit
67 parameters, allowing us to identify circuit parameters that most strongly influence energy consumption. We then
68 show that individual neurons in the pyloric network can be tuned separately to minimize their energy consumption,
69 and thereby achieve low energy consumption at the circuit level. Finally, since the crab *Cancer borealis* is subject to
70 daily and seasonal fluctuations in temperature, we study the trade-off between metabolic cost and robustness to
71 changes in temperature [31–34]. We find that metabolic cost can vary across temperatures, but that the system can
72 be energy efficient and temperature robust at the same time.

73 Results

74 Disparate energy consumption despite similar network activity

75 We studied the metabolic cost in a model of the pyloric network (Fig. 1a). In this model, disparate sets of maximal
76 membrane and synaptic conductances can give rise to similar network activity [5]. As an example, we simulated
77 two such circuit configurations (Fig. 1b) and computed their metabolic cost using a previously described measure of
78 energy consumption [35]. In this measure, the energy for each ion channel is the time integral of the product of the
79 membrane current and the respective difference between the membrane voltage and the reversal potential. The
80 energy consumed by the entire neural circuit is the sum of the energies across channels of all neurons (details in
81 Methods).

82 Although the two simulated circuit configurations produce similar network activity, even at the single-spike level
83 (Fig. 1c), the total energy consumption (Fig. 1d) as well as the moment by moment energy consumption differ sub-
84 stantially (Fig. 1e). A closer inspection of the energy consumed by each current in the PY neuron during the action
85 potentials [36] shows that the difference in energy between these two network configurations is also evident in the
86 energy consumed by the sodium current Na, the delayed-rectifier potassium current Kd, and the transient calcium

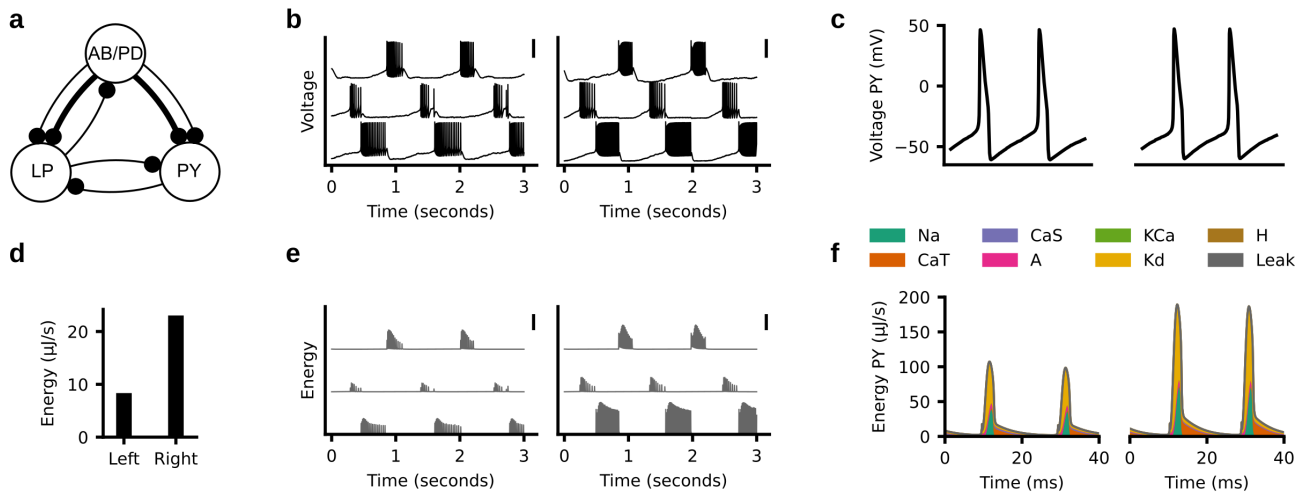


Figure 1. Similar activity with different energy consumption. (a) Computational model of the pyloric network consisting of three model neurons (AB/PD, LP, PY) and seven synapses. (b) Traces with similar circuit activity (traces from top to bottom: AB/PD, LP, PY) despite different circuit parameters (parameter values not plotted). Scale bars indicate 50 mV. (c) Close-up of two spikes in the PY neural activity shown in (b). (d) Total energy consumption divided by the duration of the simulation (10 seconds) for the traces shown in (b). The left trace has 3-fold lower metabolic cost than the right trace. (e) Consumed energy at each time point. Scale bar indicates 100 $\mu\text{J/s}$. (f) The energy consumed by each of the ion currents during the two spikes shown in (c).

87 current CaT (Fig. 1f).

88 Disparity in energy consumption in models matching experimental data

89 The example above illustrates that the model of the pyloric network can, in principle, produce the same activity with
 90 different metabolic costs. However, it is unclear how broad the range of metabolic costs associated with the same
 91 network output is. In order to address this, we need to identify the full space of maximal membrane and synaptic
 92 conductances (31 parameters in total) that match experimental measurements of network activity and to characterise
 93 the energy consumption of each of these configurations.

94 We used a recently introduced machine learning tool for simulation-based inference, Sequential Neural Posterior
 95 Estimation (SNPE) [13], to estimate the set of circuit parameters (the posterior distribution) consistent with data and
 96 prior assumptions about the parameters. In SNPE, random parameters which specify network configurations are
 97 initially sampled from the prior distribution (in our case a uniform distribution within plausible parameter ranges)
 98 and used to simulate network activity. Subsequently, a neural-network based density estimator is trained on these
 99 simulated network activities to learn which parameter sets produce network activity that is compatible with empirical
 100 observations. In order to generate the training data for the neural network, SNPE requires millions of model simu-
 101 lations to accurately infer the set of data-compatible parameters. To improve the simulation efficiency and make
 102 the neural network predict parameter sets that more closely match experimental data, we introduced a modification
 103 of the algorithm (Fig. 2a): A technical challenge for SNPE is that parameter sets sampled from the prior distribu-
 104 tion might produce simulation results that are not ‘valid’, i.e. produce clearly non-sensible data: E.g., if there are no
 105 bursts, phase gaps between bursts are not defined (Fig. 2a, forth panel, red). For SNPE, these ‘invalid’ simulations are
 106 discarded immediately. In order to reduce the fraction of simulations that are discarded, we introduce a classifier
 107 to predict whether a parameter set will lead to a ‘valid’ or an ‘invalid’ simulation output [30] (Fig. 2a, second panel).
 108 Once the classifier is trained on an initial set of simulations, parameters are immediately discarded without running
 109 the simulation, if the classifier confidently predicts that the simulation will be invalid (details in Methods). We name
 110 the distribution of parameters that are accepted by the classifier the ‘restricted prior’ (Fig. 2a, third panel). Once
 111 sufficiently many valid simulations are performed, SNPE proceeds by training a deep neural density estimator to es-
 112 timate the posterior distribution over parameters of the model [13] (Fig. 2a, last two panels, proof of convergence to
 113 the correct posterior distribution in Methods).

114 We used this procedure to infer the posterior distribution over maximal membrane and synaptic conductances
 115 of the model of the pyloric network given salient and physiologically relevant features of experimentally measured

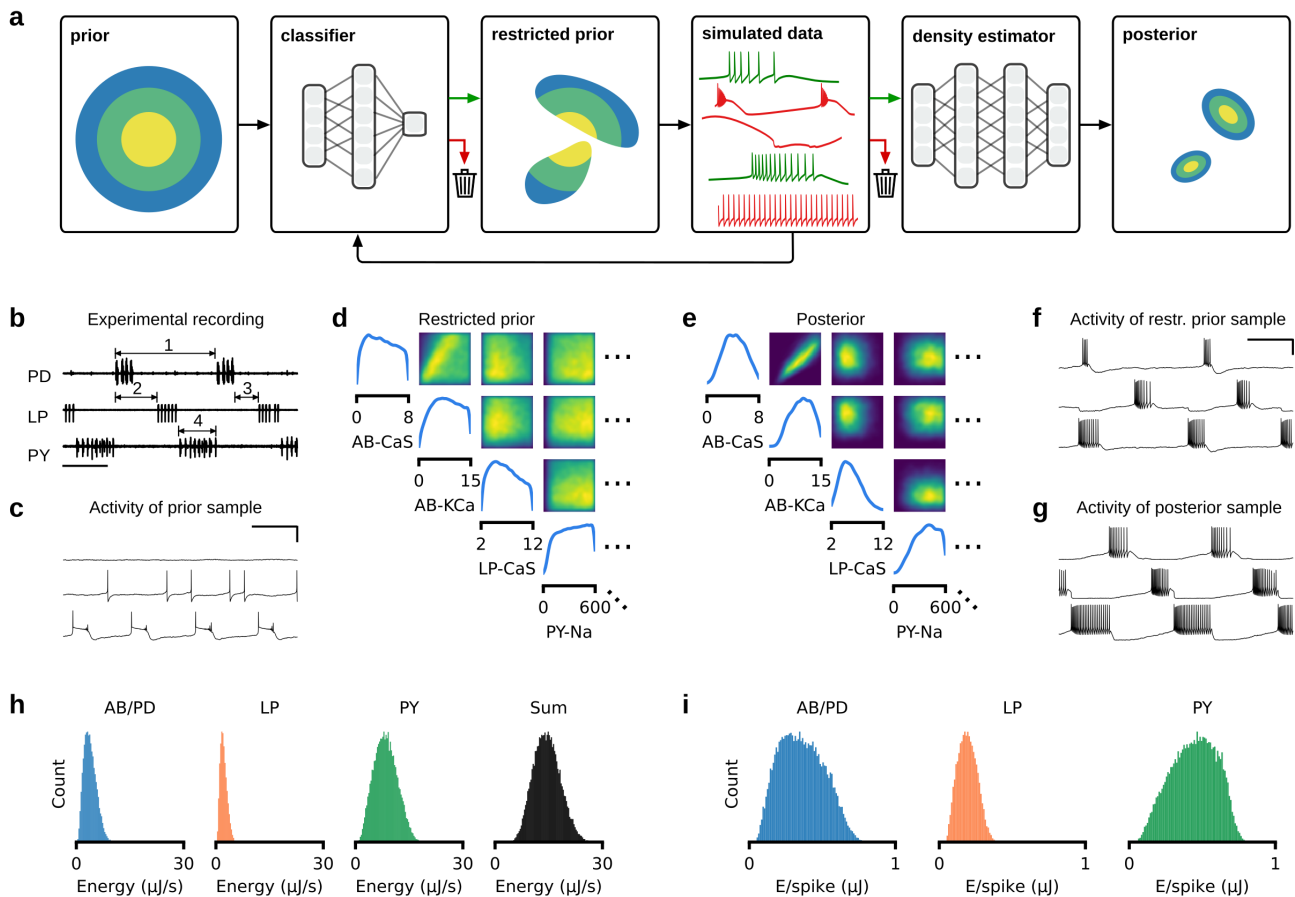


Figure 2. Bayesian inference reveals wide range of energy consumption. (a) Inferring the posterior distribution by combining a rejection classifier and a deep neural density estimator. First, a classifier (trained on an initial set of simulations) predicts which circuit parameters sampled from the prior produce ‘valid’ simulation outputs. We then proceed by sampling from the part of the parameter space that is accepted by the classifier, i.e. the ‘restricted prior’. All ‘valid’ data (green) are used to train a deep neural density estimator, all ‘invalid’ data are discarded (red) [13]. Once this estimator is trained, it can be evaluated on experimental data to return the posterior distribution over model parameters. (b) Experimental data recorded from the pyloric network [37]. Arrows indicate a subset of the physiologically relevant features, namely the cycle period (1), phase delays (2), phase gaps (3), and burst durations (4) (see Methods for details). (c) Simulation output from a parameter set sampled from the prior distribution. The traces are: AB/PD (top), LP (middle), PY (bottom). Scale bars correspond to 500 ms and 50 mV. (d) Subset of the marginals and pairwise marginals of the 31-dimensional restricted prior, i.e. the subspace of parameters for which the model produces bursting activity. All maximal conductances are given in mS/cm^2 . (e) Subset of the marginals and pairwise marginals of the posterior distribution, i.e. the subspace of parameters for which the model matches experimental data shown in panel (b) (full posterior distribution in Appendix 1 Fig. 1). (f) Sample from the restricted prior producing bursting activity but not matching experimental data. (g) Sample from the posterior distribution closely matching features of the experimental data. (h) Histograms over energy consumed by each neuron (blue, orange, green) as well as by entire circuit (black). Trace with lowest energy consumes 9 times less energy than trace with highest energy. (i) Same as in (h), but for energy per spike.

116 data. These features are the cycle period, burst durations, duty cycles, phase gaps, and phase delays of the triphasic
 117 rhythm (Fig. 2b, details in Methods) [37]. Following the definitions established in previous studies [4, 5], we did not
 118 constrain the number of spikes or the spike shapes. Below, we describe the results obtained for a specific experimen-
 119 tal preparation. We qualitatively reproduced all results with two additional experimental preparations (Appendix 1
 120 Fig. 9, Appendix 1 Fig. 10, Appendix 1 Fig. 11, Appendix 1 Fig. 12, Appendix 1 Fig. 13, Appendix 1 Fig. 14) [37].

121 When simulating the pyloric network model with parameter sets sampled from the prior distribution, 99% of
 122 simulations do not produce spikes or bursts and hence characteristic summary features of the circuits are not defined
 123 (Fig. 2c). The restricted prior (Fig. 2d) is narrower than the prior distribution, but considerably broader than the
 124 posterior (Fig. 2e, full posterior distribution in Appendix 1 Fig. 1; comparison between prior, restricted prior, and
 125 posterior in Appendix 1 Fig. 2). Parameters sampled from the restricted prior often produce activity with well-defined

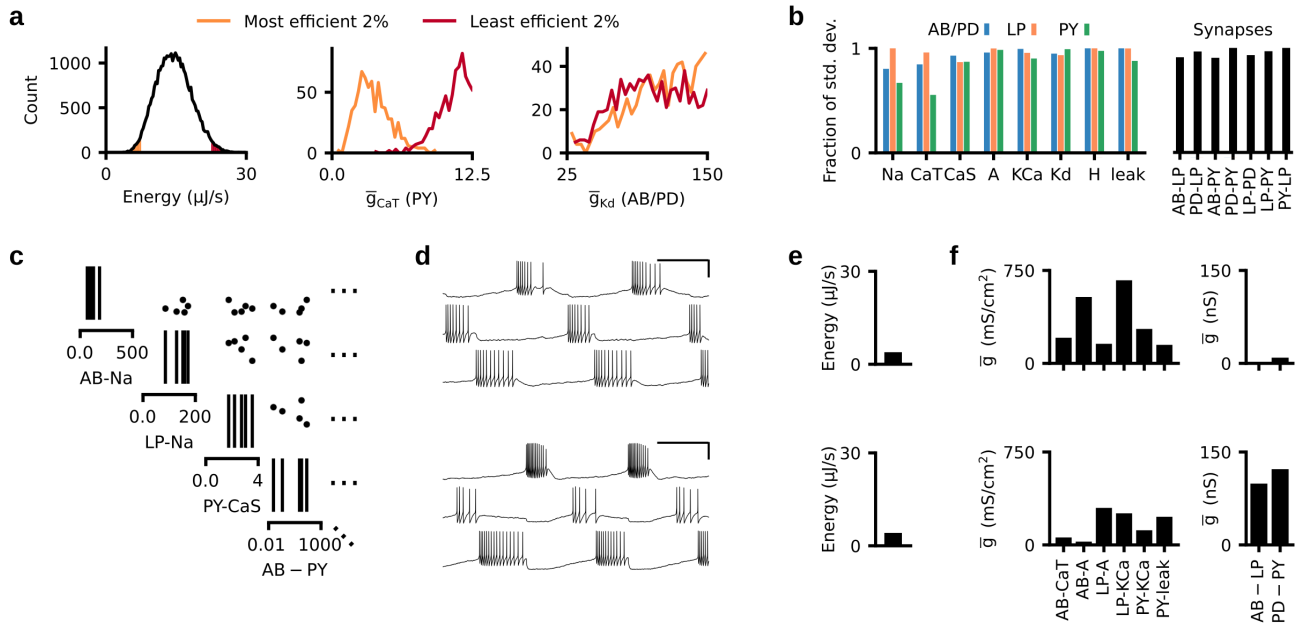


Figure 3. Metabolic constraints on individual circuit parameters. (a) Left: Energy consumption of 35,939 models that match experimental data. The orange area corresponds to the energy consumption in the lowest 2% quantile, red area to the top 98% quantile. Middle: Distribution of the maximal conductance of the transient calcium channel (CaT) in the PY neuron in the 2% (orange) and 98% quantile (red). Right: Distribution of the maximal conductance of the delayed-rectifier potassium channel (Kd) in the AB/PD neuron in the 2% (orange) and 98% quantile (red). (b) Standard deviation of parameters for models with energy consumption in the lowest 2% quantile. Standard deviation is normalized to the standard deviation of the parameters across all 35,939 models in our database. (c) Subset of the parameter values of the five most efficient circuit configurations in our database. (d) The network activity produced by two of these five configurations. Scale bar indicates 500 ms and 50 mV. (e) The energy consumption of the two configurations shown in panel (d). (f) Subset of circuit parameters of the two solutions shown in panel (b). Despite similar network activity and low energy consumption, several parameters differ by more than 2-fold. The membrane conductances are scaled by the following factors (left to right): 100, 10, 10, 100, 100, 10000.

126 summary features (Fig. 2f), but do not generally match experimental data, whereas samples from the posterior closely
 127 match experimental data (Fig. 2g). By using the classifier to reject ‘invalid’ simulations, we required half as many
 128 simulations compared to ‘classical’ SNPE [13] and achieved a higher accuracy (Appendix 1 Fig. 3). For the subsequent
 129 analyses, we only considered posterior samples whose activity was within a prescribed distance to the experimental
 130 data, and discarded all other samples (details in Methods). We simulated 1 million parameter configurations sampled
 131 from the posterior, out of which approximately 3.5% fulfilled the distance criterion, leading to a database of 35,939
 132 parameter sets whose activity closely matched experimental data. Sampling from the prior distribution rather than
 133 the posterior would have required approximately 600 billion simulations to obtain 35,939 parameter sets that fulfill
 134 our criterion (60,000 times more than with our method).

135 We computed the energy consumption of each of the 35,939 circuit activities (Fig. 2h). The circuit configuration
 136 with lowest total energy consumes nine times less energy than the circuit configuration with highest total energy.
 137 To ensure that the difference in energy does not only stem from different numbers of spikes within a burst, we also
 138 computed the average energy consumed during a spike (energy per spike) in each of the neurons (Fig. 2i). As with total
 139 energy, energy per spike strongly varies across parameter configurations. These results show that, despite similar
 140 circuit function, different parameter sets can have vastly different energy consumption. Below, we investigate the
 141 mechanisms giving rise to this phenomenon.

142 Metabolic constraints on individual circuit parameter ranges

143 How strongly does enforcing low energy consumption constrain the permissible ranges of circuit parameters? We
 144 inspected the circuit parameters of the 2% most and least efficient configurations within our database of 35,939
 145 model configurations (Fig. 3a, left). For some circuit parameters, the range of values producing efficient activity is
 146 clearly different from the range of values producing energetically costly activity (e.g. the maximal conductance of the

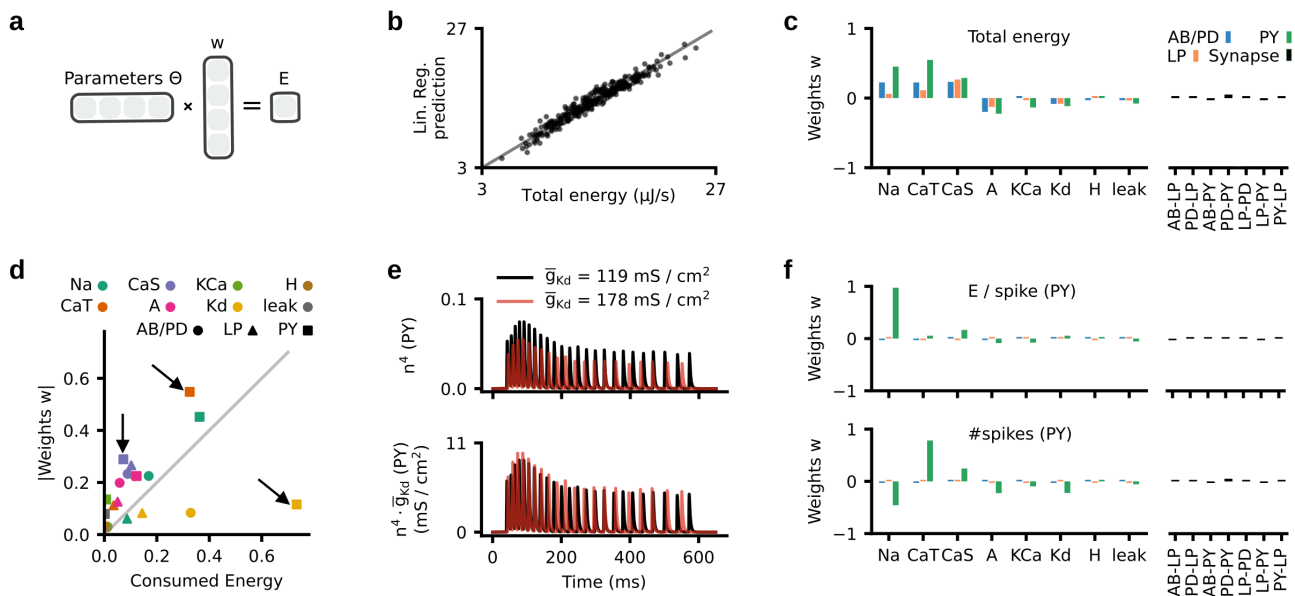


Figure 4. Influence of circuit parameters on energy consumption. (a) Illustration of linear regression from circuit parameters Θ (taken from our database of 35,939 configurations) onto energy consumption E . (b) The linear regression accurately predicts the energy consumption on a test set of 300 circuit configurations (black dots). Grey line is the identity function. (c) Weights w of the linear regression. Left: Weights of the maximal membrane conductances. Right: Weights of the maximal synaptic conductances. (d) Weights w as a function of energy consumption (both normalized), for all membrane currents (arrows highlight three illustrative examples). Membrane conductances on the top left consume little energy, but their maximal conductances correlate strongly with energy consumption. Conductances on the bottom right consume a lot of energy, but their maximal conductances correlate weakly with energy consumption. (e) Top: The gating variable n^4 of the Kd current in the PY neuron during activity produced by two circuit configurations (black and red) which are identical apart from the magnitude of \bar{g}_{Kd} . Bottom: The product of gating variable and maximal conductance $n^4 \cdot \bar{g}_{Kd}$ for the same configurations. (f) Top: Weights of a linear regression onto the energy per spike in the PY neuron. Bottom: Weights of a linear regression onto the number of spikes in the PY neuron.

147 transient calcium current in the PY neuron, Fig. 3a, middle). For other parameters, the range does not change (e.g. the
 148 maximal conductance of the delayed-rectifier potassium current in the AB/PD neuron, Fig. 3a, right). To quantify how
 149 strongly low energy consumption constrains parameters, we compared the parameter standard deviation across
 150 all 35,939 model configurations to that of the most efficient 2% (Fig. 3b). Most parameters in the circuit barely get
 151 constrained by energy consumption (values close to one in Fig. 3b). The parameters that get constrained the most by
 152 enforcing low energy consumption are the Na and CaT conductances of the AB/PD neuron, the CaS conductance of
 153 the LP neuron, and the Na, CaT, CaS, and leak conductances of the PY neuron. However, for all of these parameters,
 154 a large fraction of variability remains.

155 In order to ensure that the remaining variability of circuit parameters does not stem from the remaining variabil-
 156 ity of energy consumptions within the lowest 2% quantile, we inspected the five most efficient configurations in our
 157 database of 35,939 model configurations. Even these five circuit configurations have strongly disparate circuit param-
 158 eters (Fig. 3c). Despite having similar activity (Fig. 3d) and very low (and similar) metabolic cost (Fig. 3e), their circuit
 159 parameters are disparate (Fig. 3f). These results demonstrate that metabolic efficiency constrains the range of some
 160 circuit parameters, but it is possible to achieve low metabolic cost and similar network activity with widely disparate
 161 circuit parameters.

162 Conductances of energetically costly channels do not necessarily correlate with energy consump- 163 tion

164 We wanted to understand how each circuit parameter affects energy consumption. We performed a linear regression
 165 from circuit parameters (taken from our database of 35,939 model configurations) onto the energy consumption of
 166 these circuits (Fig. 4a). This linear regression achieved a high accuracy, demonstrating that energy consumption
 167 can be linearly predicted from circuit parameters (Fig. 4b; a non-linear regression with a neural network leads to

168 similar results and is shown in Appendix 1 Fig. 4; details in Methods). The regression weights w indicate how strongly
169 energy consumption is correlated with each parameter value (Fig. 4c). The maximal sodium conductance \bar{g}_{Na} and the
170 transient calcium conductance \bar{g}_{CaT} of the AB/PD and PY neuron as well as the slow calcium conductance \bar{g}_{CaS} of the
171 AB/PD, LP, and PY neuron are most strongly correlated with energy consumption: Increases of these conductances are
172 associated with an increase in energy consumption, and thus, small conductance values correspond to metabolically
173 more efficient solutions. The synaptic conductances are weakly correlated with energy consumption, which can be
174 explained by the low values of the maximal synaptic conductances: The synaptic strengths range up to 1000 nS,
175 whereas the membrane conductances can range up to 0.4 mS (i.e. $4 \cdot 10^5$ nS), such that synapses consume only
176 0.08% of the total energy in the circuit. These results demonstrate that energy consumption can be linearly predicted
177 from circuit parameters, and that energy consumption is most strongly correlated with the maximal conductances
178 of sodium as well as slow and transient calcium.

179 How do different currents affect total energy consumption? Do they directly consume energy, or do they trigger
180 processes that then require energy? We addressed these questions by comparing the fraction of energy consumed
181 by each current (as defined by our measure of energy [35], Fig. 1f) to the linear regression weight w associated with
182 its maximal conductance (Fig. 4d). We found that some currents consume a lot of energy, although their maximal
183 conductances barely correlate with energy consumption, e.g. the Kd current in the PY neuron (Fig. 4d, bottom right
184 arrow), while other currents consume little energy, but nonetheless their maximal conductances are correlated with
185 energy consumption, e.g. the CaS and CaT currents of the PY neuron (Fig. 4d, top left arrows).

186 We investigated the neuronal mechanisms that give rise to these behaviors. First, to understand how currents
187 can consume large amounts of energy despite their maximal conductance only weakly correlating with energy, we
188 investigated the effects of the delayed-rectifier potassium conductance \bar{g}_{Kd} on circuit activity. We simulated two circuit
189 configurations, identical apart from the magnitude of \bar{g}_{Kd} in the PY model neuron. In the configuration with higher
190 \bar{g}_{Kd} , the gating variable n did not reach as high values as for the other configuration, thus leading to a similar effective
191 conductance $n^4 \cdot \bar{g}_{Kd}$ (Fig. 4e). This demonstrates that changes in the maximal conductance \bar{g}_{Kd} only weakly influence
192 the current and thereby the energy consumption. Thus, despite the potassium current consuming a lot of energy
193 due to a large flow of ions (compared to other channels), its maximal conductance \bar{g}_{Kd} only weakly correlates with
194 energy consumption. Second, to understand how maximal conductances can correlate with energy consumption
195 despite their channels consuming little energy, we disentangled the correlation of circuit parameters with energy
196 consumption into two parts: The energy *per spike* and the number of spikes. We fitted two additional linear regression
197 models: One regression from circuit parameters onto number of spikes in the PY neuron and one regression from
198 circuit parameters onto energy per spike in the PY neuron. We again find good predictive performance of these
199 models, showing that the energy per spike and the number of spikes can also be linearly predicted from circuit
200 parameters (regression performance in Appendix 1 Fig. 5). The energy per spike is strongly correlated with the sodium
201 conductance (Fig. 4f, top), whereas the number of spikes is most strongly correlated with the maximal conductance
202 of transient calcium (also with sodium, slow calcium, and transient potassium conductances, Fig. 4f, bottom). This
203 demonstrates that increases in the maximal conductance of transient calcium lead to a higher number of spikes,
204 which involve increased energy consumption through other currents. We verified this hypothesis by simulating two
205 configurations that were identical apart from the magnitude of \bar{g}_{CaT} in the PY model neuron and found that the
206 configuration with higher \bar{g}_{CaT} indeed produced more spikes per burst. This shows that, despite the calcium channel
207 consuming little energy itself, increasing \bar{g}_{CaT} can lead to higher energy consumption by increasing the number spikes,
208 which involve energy consumption through other currents (mostly sodium and potassium). Overall, our analyses
209 demonstrate that currents which consume a lot of energy are not necessarily the ones which influence energy the
210 most.

211 **Neurons can be tuned individually to achieve minimal circuit energy**

212 We wondered how single neurons interact to produce functional and efficient circuit activity. Can the energy of the
213 entire circuit be minimized by optimizing the energy of each neuron individually? And does the circuit retain functional
214 activity when neurons are individually optimized for low energy efficiency? Within our database of 35,939 model
215 configurations, there is a weak correlation between the energies consumed by pairs of neurons, which suggests
216 that the energy consumption between neurons might be independent from one another (Fig. 5a; AB/PD versus LP,
217 correlation coefficient $r = -0.006$, p-value $p = 0.23$; LP versus PY, $r = 0.02$, $p = 3 \cdot 10^{-6}$; AB/PD versus PY, $r = -0.03$, $p =$

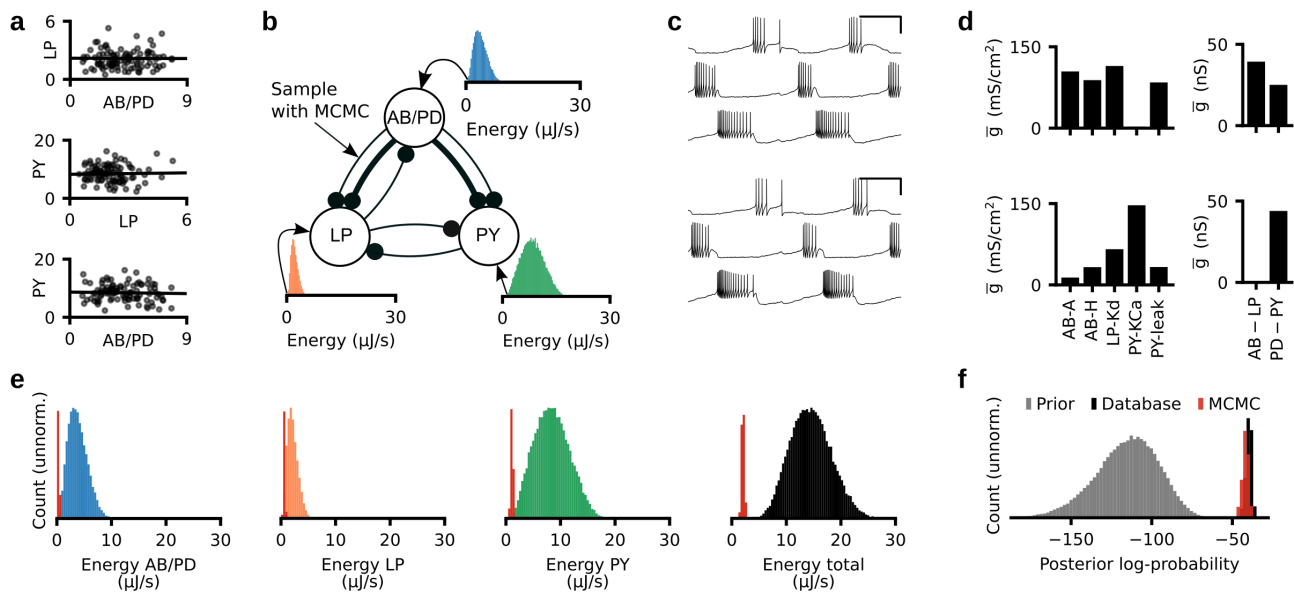


Figure 5. Neurons can be tuned individually to achieve minimal circuit energy consumption. (a) Black dots: Energy consumed by each neuron separately. 100 randomly selected parameter configurations from our database of 35, 939 configurations. Black line: Linear regression shows a weak correlation between the energy consumed by pairs of neurons. (b) We select the five most efficient parameter configurations for each neuron separately, and search with Markov chain Monte Carlo (MCMC) for synaptic conductances such that the target circuit activity is achieved. (c) The activity produced by two parameter configurations produced with the strategy described in (b). (d) A subset of the membrane (left) and synaptic (right) conductances for the configurations in panel (c). Despite generating similar network activity, the configurations have very different circuit parameters. The membrane conductances are scaled with the following factors (left to right): 10, 10000, 1, 100, 10000. (e) Histogram over the energy consumption of all 35, 939 models in our database (blue, orange, green, black) and the energy consumption of the configurations produced with the strategy described in panel (b) (red). (f) Histogram of the posterior log-probability for samples from the prior distribution (grey), for the 35, 939 models in our database (black), and for the configurations produced with the strategy described in panel (b) (red).

218 $8 \cdot 10^{-9}$). We thus investigated whether we could optimize the parameters of each neuron individually for low energy
 219 consumption and still retain functional circuit activity. We searched our database of 35, 939 model configurations for
 220 the single neuron models with minimal energy consumption individually. We selected the five most efficient single
 221 neuron parameter combinations for each of the neurons and assembled them into 125 (5^3) network configurations.
 222 We then identified synaptic conductances that match each of these configurations with Markov chain Monte Carlo
 223 (Fig. 5b, details in Methods). Notably, given the already estimated full posterior distribution, this step does not require
 224 additional simulations.

225 For each of the 125 combinations of membrane conductances, we found a set of synaptic conductances for which
 226 the network activity closely resembles experimentally measured activity (Fig. 5c). The resulting configurations have
 227 disparate parameters (Fig. 5d) but highly similar network activity. Furthermore, we found that the resulting configura-
 228 tions have similar and very low energy consumption. The energy consumption of these circuits is significantly smaller
 229 than that of any of the configurations in our database of 35, 939 model configurations (Fig. 5e). This demonstrates
 230 that optimizing a specific neuron for energy efficiency does not preclude the connected neurons from being energy
 231 efficient. Thus, our results suggest that the pyloric network can be optimized for energy efficiency by tuning neurons
 232 individually for low energy consumption.

233 We estimated how likely are these energy-efficient circuits under the estimated posterior. We found that all these
 234 models have similar posterior log-probability as the 35, 939 model configurations in our database (Fig. 5f), i.e. these
 235 are as likely to underlie the experimentally measured activity as the database models. Thus, the low-energy confi-
 236 gurations were not sampled when generating our original model database because of the high dimensionality of the
 237 parameter space, and we cannot exclude the possibility that there might be unsampled regions in parameter space
 238 with even more energy-efficient circuit configurations.

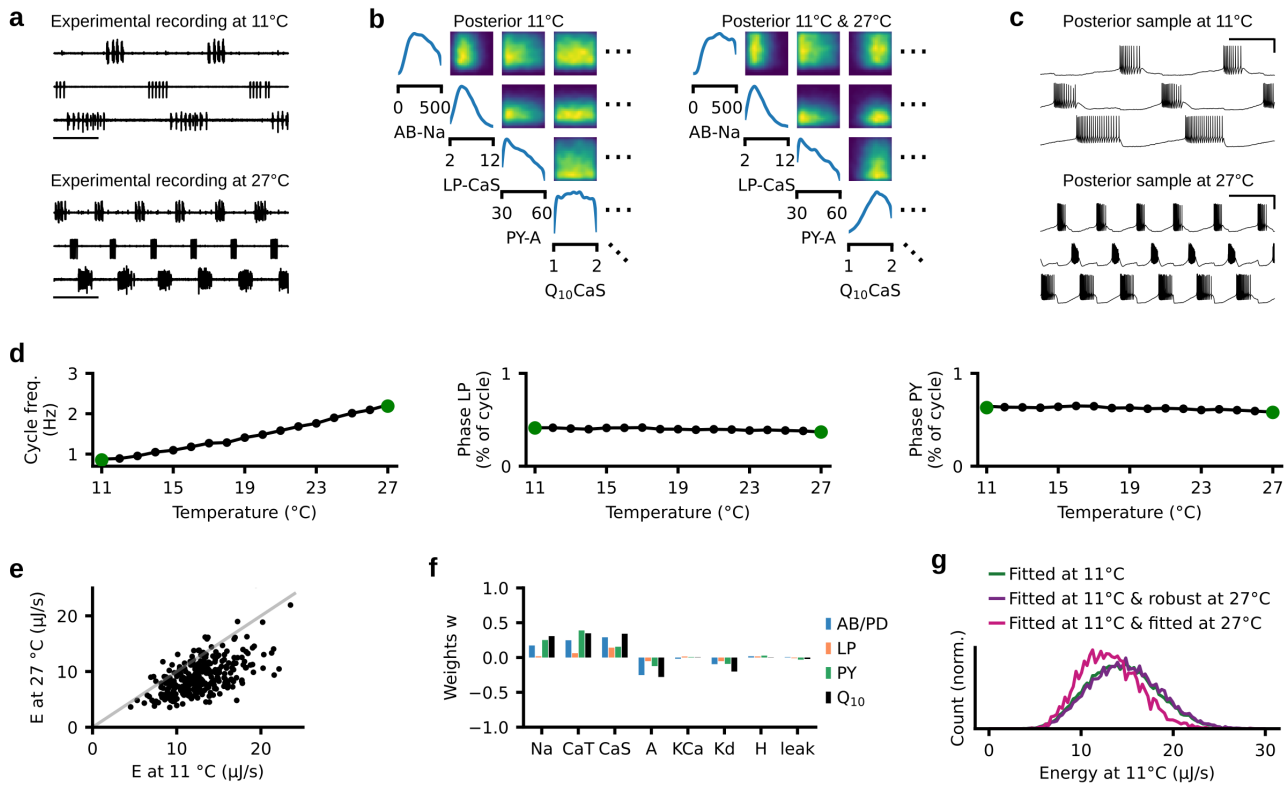


Figure 6. Temperature robustness does not preclude energy efficiency. (a) Top: Experimental data at 11°C. Bottom: Experimental data at 27°C [37]. (b) Left: Posterior distribution given experimental data at 11°C. Right: Posterior given experimental data at 11°C and 27°C. (c) Simulations for a parameter set drawn from the posterior distribution matching experimental data at 11°C and 27°C. Simulations at 11°C (top) and 27°C (bottom). (d) Cycle frequency (left), phase of LP neuron (middle) and phase of PY neuron (right) for parameter set shown in panel (c), simulated at temperatures between 11°C and 27°C. Green dots are the values of the experimental preparations. (e) Energy consumption at 11°C versus 27°C for 967 circuits sampled from the posterior (in (b) right). In grey, the identity line. (f) Influence of circuit parameters and Q_{10} values on energy consumption at 27°C. Weights w obtained by linear regression, similarly to Fig. 4. (g) Green: Distribution of the energy consumption of circuits matching experimental data at 11°C. Purple: Distribution of the energy consumption of circuits that match data at 11°C and are robust at 27°C. Pink: Distribution of the energy consumption of circuits that match experimental data at 11°C and 27°C.

239 Robustness to temperature does not require an increased metabolic cost

240 The crab *Cancer borealis* experiences daily and yearly fluctuations in temperature which in turn influence the chemical
 241 and physical properties of neurons [31–33]. Nonetheless, neural circuits such as the pyloric network can maintain
 242 their functionality in the presence of these temperature variations. As temperature increases, the cycle frequency of
 243 the circuit increases exponentially, but the phases between bursts remain relatively constant [34, 38]. We investigated
 244 whether the pyloric network trades off robustness to changes in temperature with energy efficiency, i.e. whether
 245 temperature-robust solutions are more energetically costly.

The temperature-dependence of a biophysical parameter R is captured by the Q_{10} value and is defined as follows:

$$R_T = R_{ref} Q_{10}^{(T-T_{ref})/10},$$

246 where R_{ref} is the parameter value at the reference temperature $T_{ref} = 11^\circ\text{C}$. We extended the model of the pyloric
 247 network to include Q_{10} values for all maximal membrane and synaptic conductances (details in Methods) [39, 40]. We
 248 then used SNPE to identify all maximal membrane and synaptic conductances, as well as the associated Q_{10} values
 249 (41 parameters in total) that match experimental recordings at 11°C and 27°C (Fig. 6a) [37]. We set the previously
 250 identified posterior distribution (Fig. 2e) over circuit parameters given experimental data at 11°C as the new prior
 251 distribution, and then applied SNPE to match the model with experimental data at 27°C (Fig. 6b, full posterior in Ap-
 252 pendix 1 Fig. 7, details in Methods). We sampled circuit parameters and Q_{10} values from the resulting distribution
 253 and selected samples whose activity closely matched experimental data at 11°C and 27°C (Fig. 6c). Overall, we gen-

254 erated a database of 967 sets of circuit parameters and Q_{10} values. When simulating at temperatures between 11°C
255 and 27°C, these circuits show the characteristic exponential increase in cycle frequency as well as the constant phase
256 relationship between bursts observed experimentally (Fig. 6d) [34].

257 We asked whether the energy consumed by the circuit at 11°C is proportional to the energy consumed at 27°C.
258 We found that, despite the number of spikes in our model being higher at higher temperatures, the total energy
259 consumption is lower at 27°C (Fig. 6e; note that, for one of the three preparations, the energy consumptions at 11°C
260 and 27°C are similar). This occurs because at higher temperatures, the increase in the number of spikes is accom-
261 panied by an increase in channel time constants and respective decrease in energy per spike (Appendix 1 Fig. 8). In
262 addition, there is a clear correlation between energy consumptions at 11°C and 27°C (Pearson-correlation coefficient:
263 0.66), although circuit configurations with similar efficiency at 11°C can show a range of energy consumptions at 27°C
264 (Fig. 6e). A potential reason for this range of energies at 27°C (for fixed energy at 11°C) is the influence of Q_{10} values
265 on the energy consumption. To investigate this, we performed a linear regression to predict energy consumption
266 at 27°C from circuit parameters and Q_{10} values and inspected the linear regression weights w (Fig. 6f): Indeed, Q_{10}
267 values correlate strongly with energy consumption, and the direction and magnitude of their influence follows that
268 of the corresponding maximal membrane conductances.

269 Does temperature robustness have an influence on metabolic cost? We computed the energy consumed at 11°C
270 for three different scenarios: First, for all models in our database of 35, 939 model configurations matching experimen-
271 tal data recorded at 11°C (same as Fig. 2h). Second, for all models in our database of 35, 939 model configurations
272 that are also functional at 27°C (i.e. produce triphasic activity). Third, for all models in our database of 967 model
273 configurations matching experimental data recorded at 11°C and 27°C. In all three of these scenarios, the distribu-
274 tion of metabolic cost was similar (Fig. 6g. Note that the slightly different average energy consumption between the
275 first and the third scenario occurred only in two of the three preparations, see Appendix 1 Fig. 11 and Appendix 1
276 Fig. 14). In particular, all three scenarios contained configurations that produce energy efficient circuit function. This
277 demonstrates that enforcing temperature robustness does not require the pyloric network to be less energy efficient.

278 Overall, our analyses indicate that Q_{10} values can contribute to the energy efficiency of the circuit and might,
279 therefore, be the subject of tuning for metabolic efficiency. In addition, we showed that temperature robustness
280 does not entail additional metabolic cost.

281 Discussion

282 Neural systems undergo environmental and neuromodulatory perturbations to their mechanisms. The parameter
283 degeneracy of neural systems, i.e. the ability to generate similar activity from disparate parameters, confers a certain
284 degree of robustness to such perturbations [6–9, 41, 42]. However, not all system configurations might be equally
285 desirable, with some configurations being more energy efficient than others [14]. Here, we analysed the energy
286 consumption of parameter configurations with similar activity in the pyloric network of the stomatogastric ganglion.
287 We found that, even when the network activity is narrowly tuned to experimental data, the energy consumption
288 can strongly vary between parameter configurations. Furthermore, we studied how membrane and synaptic con-
289 ductances influence energy consumption [14], and demonstrated that neurons in the pyloric network can be tuned
290 individually to achieve low energy consumption. Lastly, we showed that temperature robustness does not preclude
291 energy efficiency. These findings were facilitated by a methodological advance that increased the efficiency of previ-
292 ously published tools for simulation-based inference [13, 30, 43, 44].

293 Relation to previous work on metabolic cost of neural systems

294 There has been extensive work on quantifying the metabolic cost of biophysical processes in single neurons [14, 21,
295 22, 24–26], and how single neurons subject to functional constraints can be tuned to minimize energy consumption
296 [14, 22, 25]. However, so far, it has been unclear how energy efficiency impacts the parameter degeneracy of neural
297 systems. While a plausible hypothesis would have been that energy efficiency reduces or eliminates degeneracy
298 altogether, here we found that parameter degeneracy is preserved for most parameters, even within circuits with
299 highly similar energy consumption. Nevertheless, we should note that our findings are based on two simplifying
300 assumptions: First, we studied simple single-compartment neurons rather than more realistic multi-compartment
301 neuron models [45]; and second, the energy measure is derived directly from the Hodgkin-Huxley model [35], rather
302 than taking into account all the complexity of the ionic exchange leading to ATP consumption [14, 20, 22, 25].

303 Which circuit parameters influence energy consumption the most? Consistent with previous work at the single
304 neuron level, we found that total energy consumption of the pyloric network is strongly influenced by the sodium
305 current [25], but also by the transient and slow calcium currents. The maximal sodium conductance is the most
306 prominent driver of the energy per spike: Increases in the conductance lead to an increase of metabolic cost per
307 spike [14, 25]. In contrast, calcium currents influence energy consumption through the number of spikes within
308 a burst, despite not consuming much energy themselves. Our results suggest that the maximal conductances of
309 sodium and calcium might be regulated for metabolic efficiency. We thus predict that these conductances are less
310 variable in nature than expected by computational models only matching network activity.

311 Previous studies have demonstrated that synaptic mechanisms can consume a substantial amount of energy
312 [20, 46, 47]. In contrast, in the considered model of the pyloric network, synaptic currents consume only a minor
313 fraction of energy (approximately 0.08% of the total energy is consumed by synapses, whereas Attwell and Laughlin
314 [20] report 40% of energy per action potential being consumed by synaptic mechanisms). This difference is largely
315 due to the low number of connections in the pyloric network [48]: Each neuron projects to up to two other model
316 neurons, whereas the synaptic energy consumption reported in Attwell and Laughlin [20] is based on the assumption
317 of 8000 synaptic boutons per neuron. Thus, models of more complex neural circuits driven by excitatory, recurrent
318 connectivity, such as the ones found in the cortex, might spend a larger fraction of energy on synaptic mechanisms.

319 **Interplay between metabolic cost and robustness to perturbations**

320 Neural circuits are likely constrained by energy consumption, but also by other requirements, e.g. robustness to per-
321 turbations such as fluctuations in temperature or pH [34, 39, 40, 49–53]. We investigated the interplay between energy
322 consumption and temperature robustness. Consistent with previous work in a single neuron model of the grasshop-
323 per [27], we found that temperature robustness does not require an increased metabolic cost. Whether these results
324 will generalize with the inclusion of the robustness to additional external perturbations, e.g. pH fluctuations [52, 54],
325 or internal perturbations, e.g. neuromodulation [38], remains a subject for future work.

326 **Increasing the efficiency of simulation-based inference**

327 We used a previously introduced tool, SNPE [13, 44] to identify all models consistent with experimentally measured
328 activity as well as prior knowledge about realistic parameter ranges. We improved the efficiency of the method by
329 introducing a classifier that rejects ‘invalid’ simulations [30]. By using this classifier, we were able to improve the
330 accuracy of SNPE while requiring only half as many simulations [13]. Because of this larger simulation-budget, the
331 resulting posterior distributions became more accurate.

332 Generally, the classifier-enhanced SNPE can be applied to other modelling studies in neuroscience. In particular,
333 the classifier to predict ‘invalid’ simulations is valuable whenever there are parameter values for which the computa-
334 tional model of interest produces ill-defined features: E.g. the spike shape cannot be defined in cases where a neuron
335 model does not produce spikes. Our method has the potential to significantly speed up inference in these scenarios.

336 Another way of increasing simulation efficiency is to perform inference over multiple ‘rounds’ [30, 44, 55]. These
337 methods use a previous estimate of the posterior distribution to guide new simulations into regions of high posterior
338 probability. However, using the previous estimate of the posterior distribution requires changing the loss function,
339 which can make neural network training unstable [44, 56]. In contrast, using a thresholded classifier does not require
340 the algorithm to adjust the loss function, leading to more robust results and allowing it to be applied to a larger range
341 of models of neural dynamics (details in Methods). In addition, unlike in multi-round SNPE, the resulting posterior
342 distribution is amortized—it can be evaluated at new data traces without running new simulations or training a new
343 neural network. Compared to multi-round SNPE, the main drawback of the classifier approach is that simulations
344 are run from a relatively large region in parameter space (all parameter sets that might produce ‘valid’ simulation
345 outputs), whereas multi-round SNPE is tailored to a specific experimental trace and can hence be more efficient in
346 the number of required simulations.

347 **Implications for the operation of neural circuits**

348 Our findings suggest that neural circuits can show a range of possible metabolic costs, depending on the underlying
349 biophysical parameters, even with highly specific functional requirements under constant perturbations. This raises

350 the question of whether such diversity of metabolic costs is present in real biological systems, or whether and how
351 these systems are tuned for metabolic efficiency.

352 **Acknowledgments**

353 We thank Sara A. Haddad and Eve Marder for sharing their data and discussions, Martin Stemmler for discussions,
354 and Poornima Ramesh, Richard Gao, and Jan Boelts for discussions and comments on the manuscript. The authors
355 thank the International Max Planck Research School for Intelligent Systems (IMPRS-IS) for supporting MD. This work
356 was supported by the German Research Foundation (DFG) through SFB 1089 'Synaptic Microcircuits' and Germany's
357 Excellence Strategy – EXC-Number 2064/1 – Project number 390727645 as well as the German Federal Ministry of
358 Education and Research (BMBF, project 'ADIMEM', FKZ 01IS18052 A-D) to JHM.

359 Methods

360 Code availability

361 Code to reproduce the figures is available at https://github.com/mackelab/stg_energy. Code for running SNPE and
362 training a classifier to reject 'invalid' simulations is available in our toolbox: <https://github.com/mackelab/sbi>. A tutorial
363 for how to use these features can be found on our website <https://mackelab.org/sbi>.

364 Data from the crustacean stomatogastric ganglion

365 We analyzed extracellular recordings of the stomatogastric motor neurons that are involved in the triphasic pyloric
366 rhythm in the crab *Cancer borealis* [37]. The first dataset as seen in Fig. 2 and Fig. 6 is from files 845_082_0044 and
367 845_082_0064, preparation 1. The second dataset as seen in Appendix 1 Fig. 9 and Appendix 1 Fig. 11 is from files
368 857_016_0049 and 857_016_0069, preparation 1. The third dataset as seen in Appendix 1 Fig. 12 and Appendix 1
369 Fig. 14 is from files 845_078_0027 and 845_078_0040, preparation 2. All preparations were decentralized, i.e. the ax-
370 ons of the descending modulatory inputs were severed. The data were recorded at 11°C and 27°C. Full experimental
371 details in Haddad and Marder [38].

372 Circuit model of the crustacean stomatogastric ganglion

The circuit model of the crustacean stomatogastric ganglion was adapted from Prinz et al. [5]. The model is composed
of three single-compartment neurons, AB/PD, LP, and PY, where the electrically coupled AB and PD neurons are
modeled as a single neuron. Each of the model neurons contains 8 currents, a Na⁺ current I_{Na} , a fast and a slow
transient Ca²⁺ current I_{CaT} and I_{CaS} , a transient K⁺ current I_A , a Ca²⁺-dependent K⁺ current I_{KCa} , a delayed rectifier K⁺
current I_{Kd} , a hyperpolarization-activated inward current I_H , and a leak current I_{leak} . In addition, the model contains 7
synapses. As in Prinz et al. [5], these synapses are simulated using a standard model of synaptic dynamics [57]. The
synaptic input current into the neurons is given by $I_s = \bar{g}_s s (V_{post} - V_s)$, where \bar{g}_s is the maximal synapse conductance,
 V_{post} the membrane potential of the postsynaptic neuron, and V_s the reversal potential of the synapse. The dynamics
of the activation variable s are given by

$$\frac{ds}{dt} = \frac{\bar{s}(V_{pre}) - s}{\tau_s},$$

with

$$\bar{s}(V_{pre}) = \frac{1}{1 + \exp((V_{th} - V_{pre})/\delta)} \quad \text{and} \quad \tau_s = \frac{1 - \bar{s}(V_{pre})}{k_-}.$$

373 Here, V_{pre} is the membrane potential of the presynaptic neuron, V_{th} is the half-activation voltage of the synapse, δ
374 sets the slope of the activation curve, and k_- is the rate constant for transmitter-receptor dissociation rate.

375 As in Prinz et al. [5], we model two types of synapses, since AB, LP, and PY are glutamatergic neurons whereas PD
376 is cholinergic. We set $E_s = -70$ mV and $k_- = 1/40$ ms for all glutamatergic synapses and $E_s = -80$ mV and $k_- = 1/100$
377 ms for all cholinergic synapses. For both synapse types, we set $V_{th} = -35$ mV and $\delta = 5$ mV. The membrane area is
378 $0.628 \cdot 10^{-3}$ cm².

379 For each set of membrane and synaptic conductances, we numerically simulate the circuit for 10 seconds with a
380 step size of 0.025 ms. At each time step, each neuron receives Gaussian noise with mean zero and standard deviation
381 0.001 mV·ms^{-0.5}.

382 We applied SNPE to infer the posterior over 24 membrane parameters and 7 synaptic parameters, i.e. 31 parame-
383 ters in total. The 7 synaptic parameters are the maximal conductances \bar{g}_s of all synapses in the circuit, each of which is
384 varied uniformly in logarithmic domain from 0.01 nS to 1000 nS, with the exception of the synapse from AB to LP, which
385 is varied uniformly in logarithmic domain from 0.01 nS to 10000 nS. The membrane parameters are the maximal mem-
386 brane conductances for each neuron. The membrane conductances are varied over an extended range of previously
387 reported values [5, 13]: The prior distribution over the parameters [Na, CaT, CaS, A, KCa, Kd, H, leak] is uniform with
388 lower bounds $p_{low} = [0, 0, 0, 0, 0, 25, 0, 0]$ mS cm⁻² and upper bounds $p_{high} = [500, 7.5, 8, 60, 15, 150, 0.2, 0.01]$ mS cm⁻²
389 for the maximal membrane conductances of the AB neuron, $p_{low} = [0, 0, 2, 10, 0, 0, 0, 0.01]$ mS cm⁻² and $p_{high} =$
390 $[200, 2.5, 12, 60, 10, 125, 0.06, 0.04]$ mS cm⁻² for the maximal membrane conductances of the LP neuron, and $p_{low} =$
391 $[0, 0, 0, 30, 0, 50, 0, 0]$ mS cm⁻² and $p_{high} = [600, 12.5, 4, 60, 5, 150, 0.06, 0.04]$ mS cm⁻² for the maximal membrane con-
392 ductances of the PY neuron.

393 We computed 15 summary features proposed by Prinz et al. [5], and 3 additional features [13]. The features
 394 proposed by Prinz et al. [5] are 15 salient features of the pyloric rhythm, namely: Cycle period T (s), AB/PD burst
 395 duration d_{AB}^b (s), LP burst duration d_{LP}^b (s), PY burst duration d_{PY}^b (s), gap AB/PD end to LP start Δt_{AB-LP}^{es} (s), gap LP end to
 396 PY start Δt_{LP-PY}^{es} (s), delay AB/PD start to LP start Δt_{AB-LP}^{ss} (s), delay LP start to PY start Δt_{LP-PY}^{ss} (s), AB/PD duty cycle d_{AB} , LP
 397 duty cycle d_{LP} , PY duty cycle d_{PY} , phase gap AB/PD end to LP start $\Delta \phi_{AB-LP}$, phase gap LP end to PY start $\Delta \phi_{LP-PY}$, LP start
 398 phase ϕ_{LP} , and PY start phase ϕ_{PY} . Note that several of these values are only defined if each neuron produces rhythmic
 399 bursting behavior. In addition, for each of the three neurons, we computed the maximal duration of its voltage being
 400 above -30 mV. We did this as we observed—for many model simulations and in contrast with experimental data—
 401 long plateaus at around -10 mV during the bursts, and wanted to detect such traces. If the maximal duration was
 402 below 5 ms, we set this feature to 5 ms. To extract the summary features from the observed experimental data, we
 403 first found spikes by searching for local maxima above a hand-picked voltage threshold, and then extracted the 15
 404 above described features. For the experimental preparation, we set the additional 3 features to 5 ms.

405 At temperatures higher than 11°C , we include Q_{10} values to simulate the biochemical changes of the network
 406 parameters. These are defined by an Arrhenius-type factor

$$R_T = R_{ref} Q_{10}^{(T - T_{ref})/10}, \quad (1)$$

407 where R_{ref} is the parameter value at the reference temperature $T_{ref} = 11^\circ\text{C}$, and R_T is the parameter value at tem-
 408 perature T . Each maximal conductance has a different Q_{10} , but the Q_{10} value is the same across neurons [40]. We
 409 introduce one Q_{10} for the glutamatergic synapses and one for the cholinergic synapses. The prior distribution for the
 410 Q_{10} values is a uniform distribution between 1 and 2 for all maximal conductances but the hyperpolarization current,
 411 for which the prior bounds are 1 and 4 [34]. The Q_{10} values for the time constants are fixed to 2.4 for most m -gates
 412 and 2.8 for all h -gates. Following the results from Caplan et al. [39], the Q_{10} values for the m -gates of KCa and CaS as
 413 well as for the calcium buffer have lower values: 2.0 for CaS and the calcium buffer and 1.6 for KCa. The Q_{10} value for
 414 the time constants of the synapses is 1.7.

415 Energy consumption

416 To compute the energy consumption E of a specific network activity, we followed the approach of Moujahid et al. [35].
 417 For each neuron, we computed the energy as:

$$E = \int \sum_m g_m (V - V_m)^2 + \sum_s g_s (V - V_s)^2 dt, \quad (2)$$

418 where g_m is the effective conductance of channel m (i.e. the product of the respective gating variables and maximal
 419 conductance) and g_s is the effective synaptic conductance s into the specific neuron. V_m is the reversal potential of
 420 the membrane current m and V_s is the reversal potential of the synapse s . The units of energy are $[S \cdot V^2 \cdot s = J]$,
 421 where S are Siemens, V are Volt, s are seconds, and J are Joules. The total energy consumption was defined as the
 422 sum of the energy consumed by each of the three neurons. Throughout the manuscript, we report the energy per
 423 second, which we obtained by dividing the total energy consumption by the duration of the simulation (10 seconds).

424 The energy per spike was defined as the energy consumed during bursts divided by the respective number of
 425 spikes.

426 **Simulation-based inference**

427 We extended Sequential Neural Posterior Estimation [13] by using a classifier to predict ‘invalid’ simulation outputs.

428 The resulting algorithm is described in algorithm 1.

Algorithm 1: SNPE

Input: simulator with (implicit) density $p(\mathbf{x}|\theta)$, observed data \mathbf{x}_o , prior $p(\theta)$, rejection criterion $g(\mathbf{x}) \in \{0, 1\}$, classification neural network $G_\zeta(\theta)$, density family q_ϕ , neural network $F(\mathbf{x}, \phi)$, number of cycles C of classifier training, simulation count for each cycle N_c

randomly initialize ϕ, ζ

$\tilde{p}_1(\theta) := p(\theta)$

$N := 0$

for $c = 1$ **to** C **do**

for $i = 1 \dots N_c$ **do**

 sample $\theta_{N+i} \sim \tilde{p}_c(\theta)$

 simulate $\mathbf{x}_{N+i} \sim p(\mathbf{x}|\theta_{N+i})$

 evaluate whether ‘valid’ $\mathbf{r}_{N+i} = g(\mathbf{x}_{N+i})$

$N \leftarrow N + N_c$

 train $\zeta \leftarrow \arg \min_{\zeta} \sum_{j=1}^N \mathcal{L}_e(\theta_j, \mathbf{r}_j)$ // classifier training

$T \leftarrow$ Tune classifier threshold s.t. false negative rate $< 1\%$

$U(\theta) \leftarrow G_\zeta(\theta) > T$

$\tilde{p}_c(\theta) \propto U(\theta)p(\theta)$

 train $\phi \leftarrow \arg \min_{\phi} \sum_{j=1}^N \mathcal{L}_d(\theta_j, \mathbf{x}_j)$ // neural density estimator training

return $q_{F(\mathbf{x}_o, \phi)}(\theta)$

430 **Proof of convergence of SNPE with classifier**

Below, we prove that the posterior distribution inferred by our method converges to the true posterior distribution. SNPE—with the classifier—minimizes the following loss function with respect to the neural network parameters ϕ :

$$\begin{aligned} \mathcal{L}_d &= -\frac{1}{N} \sum_i \log(q_\phi(\theta_i|\mathbf{x}_i)) \\ &\xrightarrow{N \rightarrow \infty} -\mathbb{E}_{p(\theta, \mathbf{x})}[\log(q_\phi(\theta|\mathbf{x}))] \\ &= -\mathbb{E}_{U(\theta)p(\theta)p(\mathbf{x}|\theta)}[\log(q_\phi(\theta|\mathbf{x}))], \end{aligned}$$

where $U(\theta)$ is a constant $U(\theta) = c > 0$ at least on the posterior support and $U(\theta) = 0$ elsewhere. Then:

$$\begin{aligned} \mathcal{L}_d &= -\iint U(\theta)p(\theta)p(\mathbf{x}|\theta) \log(q_\phi(\theta|\mathbf{x})) \, d\theta d\mathbf{x} \\ &= -\int p(\mathbf{x}) \int U(\theta)p(\theta|\mathbf{x}) \log(q_\phi(\theta|\mathbf{x})) \, d\theta d\mathbf{x} \end{aligned}$$

Since $U(\theta) > 0$ at least on the support of $p(\theta|\mathbf{x})$:

$$\mathcal{L}_d = -\int p(\mathbf{x})c \int p(\theta|\mathbf{x}) \log(q_\phi(\theta|\mathbf{x})) \, d\theta d\mathbf{x}$$

431 Since the integrand of the integral over θ is proportional to the Kullback-Leibler-divergence between the true posterior
432 $p(\theta|\mathbf{x})$ and the inferred posterior $q_\phi(\theta|\mathbf{x})$, \mathcal{L}_d is minimized if and only if $q_\phi(\theta|\mathbf{x}) = p(\theta|\mathbf{x})$ for all \mathbf{x} on the support of $p(\mathbf{x})$.

433 **Classifier of ‘valid’ simulations**

434 The algorithm includes a classifier $U(\theta)$ trained to predict ‘valid’ simulations. We use a cross-entropy loss \mathcal{L}_e . We
435 enforce the classifier $U(\theta)$ to be constant, with $U(\theta) = c > 0$ at least on the posterior support and $U(\theta) = 0$ elsewhere:

- 436 1. In order for $U(\theta)$ to be uniform, we parameterize it as a thresholded binary classifier.
- 437 2. To ensure that $c > 0$ at least on the posterior support, we choose the classifier threshold such that there are
438 few false-negatives, i.e. the classifier accepts the parameters if these lie within the posterior support.

439 If we train the classifier $U(\theta)$ with a large enough number of simulations, so that some are ‘valid’, the trained
440 classifier includes the posterior support. In order to sample from $U(\theta)p(\theta)$, we sample from the prior over parameters
441 $p(\theta)$ and accept the sampled parameters according to the classifier output.

442 **Inference of the posterior distribution given experimental data at 11°C**

443 Overall, we performed three cycles of simulation and classifier training in order to learn the restricted prior. In the
444 first round, we simulated 3 million parameter sets sampled from the prior. Among these, only 0.97% produced ‘valid’
445 summary features. We trained a classifier to detect parameter sets leading to ‘valid’ simulation outputs. We used a
446 residual neural network with 80 hidden units, two blocks, a dropout rate of 43%, and a batchsize of 199. To deal with
447 ‘valid’/‘invalid’ unbalanced data, we subsampled ‘invalid’ samples in every epoch. We post-hoc tuned the threshold
448 of the classifier such that the ratio of false-negatives was below 1% on a held-out test set. We then drew 3 million
449 samples from the resulting restricted prior. Out of these, 5.17% produced ‘valid’ summary features. We then repeated
450 this procedure and out of 3 million simulations from the resulting restricted prior, 8.45% produced good simulations.
451 Overall, in comparison to Gonçalves et al. [13], we used half as many simulations (9 million versus 18.5 million), but
452 generated a database of ‘valid’ simulations 2.5 times larger. We then used all 438,608 ‘valid’ parameter sets to obtain
453 the posterior distribution with SNPE (see Gonçalves et al. [13] for details). As deep neural density estimator, we chose
454 a neural spline flow (NSF) [58] with 10 transform layers, each consisting of a residual block with two hidden layers,
455 each with 200 hidden units.

456 Lastly, to ensure that the activity produced by samples from the posterior closely matched experimental data, we
457 sampled 1 million parameter sets from the inferred posterior distribution and performed an additional rejection step,
458 whereby posterior samples had to produce activity within a prescribed distance to the experimental data:

- 459 • cycle duration and burst durations deviated from the experimental features by a maximum distance of 0.02
460 standard deviations of all simulations accepted by the classifier, i.e. 20.6 ms for the cycle duration, and [15.0,
461 13.5, 11.5] ms for the burst durations (of AB/PD, LP, and PY neurons).
- 462 • duty cycles, phase gaps, phase delays, and phases deviated from the experimental features by a maximum
463 distance of 0.2 standard deviations.

464 Out of 1 million samples from the posterior, 35,939 samples fulfilled all these criteria. Notably, these samples are
465 no longer unbiased samples from the posterior distribution as estimated by SNPE, but they make up a database of
466 model configurations whose activity closely matches experimental data.

467 **Regression neural network**

468 We performed a linear regression to identify the contribution of the circuit parameters to the total energy consump-
469 tion using scikit-learn [59]. In order to test the robustness of the linear regression findings, we trained a regression
470 network to identify directions in the parameter space predictive of total energy consumption. The regression network
471 had the following characteristics: A Residual Network (ResNet) with one hidden layer with 20 hidden units, ReLU ac-
472 tivation functions, and 50% dropout rate [60, 61]. We trained the network with a mean-squared error loss.

473 After training the regression network, we searched for directions that were most predictive of the network output
474 $f(\cdot)$. To do so, we followed the procedure described in Constantine [62] and computed:

$$M = \mathbb{E}_{\theta \sim p(\theta|x_o)}[\nabla_{\theta} f(\theta) \nabla_{\theta} f(\theta)^T]. \quad (3)$$

475 Intuitively, M captures how much the regression function $f(\cdot)$ changes in different directions of the parameter space,
476 computed as an expected value over posterior samples. We estimated this expected value with a Monte Carlo mean
477 over 10,000 samples from the posterior distribution. We then computed the eigenvalue decomposition of M : The

478 eigenvectors of highest eigenvalue are directions in the parameter space along which the output of the regression
479 neural network is most sensitive to changes.

480 **Sampling synaptic conductances, given energy efficient single-neuron configurations**

481 In order to investigate whether efficient single-neuron parameters could lead to efficient and robust network activ-
482 ity, we first searched our database of 35,939 network configurations for the five configurations that had the lowest
483 metabolic cost in each neuron individually. We combined these single neuron configurations to generate $5^3 = 125$
484 configurations of membrane conductances. For each of the configurations, we then sampled 1,000 synaptic configu-
485 rations from the distribution:

$$p(\theta_s | \theta_m, \mathbf{x}_o) \propto p(\theta_s, \theta_m | \mathbf{x}_o), \quad (4)$$

486 where θ_s and θ_m are the synaptic and membrane conductances, respectively. We drew these samples with Markov
487 chain Monte Carlo: Specifically, we used Slice Sampling with axis-aligned updates [63]. We then simulated each of
488 these $5^3 \cdot 1000$ configurations. 72 out of the 5^3 configurations contained at least one sample that fulfilled our (distance
489 to experimental data) criteria, and 123 configurations contained a sample that fulfilled a slightly wider criteria (allowing
490 twice as much distance from the experimental data). For the remaining two configurations, we drew another 10,000
491 samples with MCMC and for each of them found at least one configuration whose activity fulfilled the slightly wider
492 criteria. The histograms in figures Fig. 5e,f are produced with all simulations that fulfilled the narrow criteria.

493 **Posterior distribution given experimental data at 27°C**

In order to infer the posterior distribution given experimental data at 27°C, we started by sampling 3 million param-
eter sets from the 31-dimensional posterior distribution at 11°C:

$$p(\theta | \mathbf{x}_o^{11}) \propto p(\mathbf{x}_o^{11} | \theta) p(\theta).$$

We then drew 3 million sets of Q_{10} values from the prior distribution over Q_{10} values (Q_{10} prior in Methods, Circuit
model of the crustacean stomatogastric ganglion). We simulated these 3 million parameter sets at 27°C, from which
approximately 18% were 'valid' and were used to train a deep neural density estimator (see Proof of convergence of
SNPE with classifier). The hyperparameters of the neural density estimator were the same as the ones chosen for the
inference at 11°C. Since this density estimator was trained on parameters sampled from the posterior distribution at
11°C, the inferred posterior is an approximation to:

$$p(\theta | \mathbf{x}_o^{27}, \mathbf{x}_o^{11}) \propto p(\mathbf{x}_o^{27} | \theta) p(\theta | \mathbf{x}_o^{11}) \propto p(\mathbf{x}_o^{27} | \theta) p(\mathbf{x}_o^{11} | \theta) p(\theta),$$

494 where \mathbf{x}_o^{11} and \mathbf{x}_o^{27} are the features of the experimental data recorded at 11°C and 27°C, respectively. In other words,
495 the resulting posterior distribution matches prior knowledge about circuit parameters as well as experimental data
496 at 11°C and 27°C. Note that we inferred the posterior distribution at 11°C while ignoring the Q_{10} values because the
497 Q_{10} values, by definition, do not influence the circuit activity at the reference temperature (which is assumed to be
498 11°C).

499 **Metabolic efficiency at 27°C**

500 For panels Fig. 6e,f and Fig. 6g (pink plot), we analyzed 967 simulations that closely matched experimental data
501 recorded at 11°C and 27°C. For Fig. 6g (purple plot), we simulated, at 27°C, the 35,939 circuit configurations that
502 match experimental data recorded at 11°C. Out of these, 8121 were robust, i.e. displayed pyloric activity at 27°C.

503 **References**

- 504 [1] J. Golowasch, L. Abbott, and E. Marder. Activity-dependent regulation of potassium currents in an identified neuron of the
505 stomatogastric ganglion of the crab cancer borealis. *Journal of Neuroscience*, 19(20):RC33–RC33, 1999.
- 506 [2] J. Golowasch, M. S. Goldman, L. Abbott, and E. Marder. Failure of averaging in the construction of a conductance-based neuron
507 model. *Journal of neurophysiology*, 87(2):1129–1131, 2002.
- 508 [3] M. S. Goldman, J. Golowasch, E. Marder, and L. Abbott. Global structure, robustness, and modulation of neuronal models.
509 *Journal of Neuroscience*, 21(14):5229–5238, 2001.

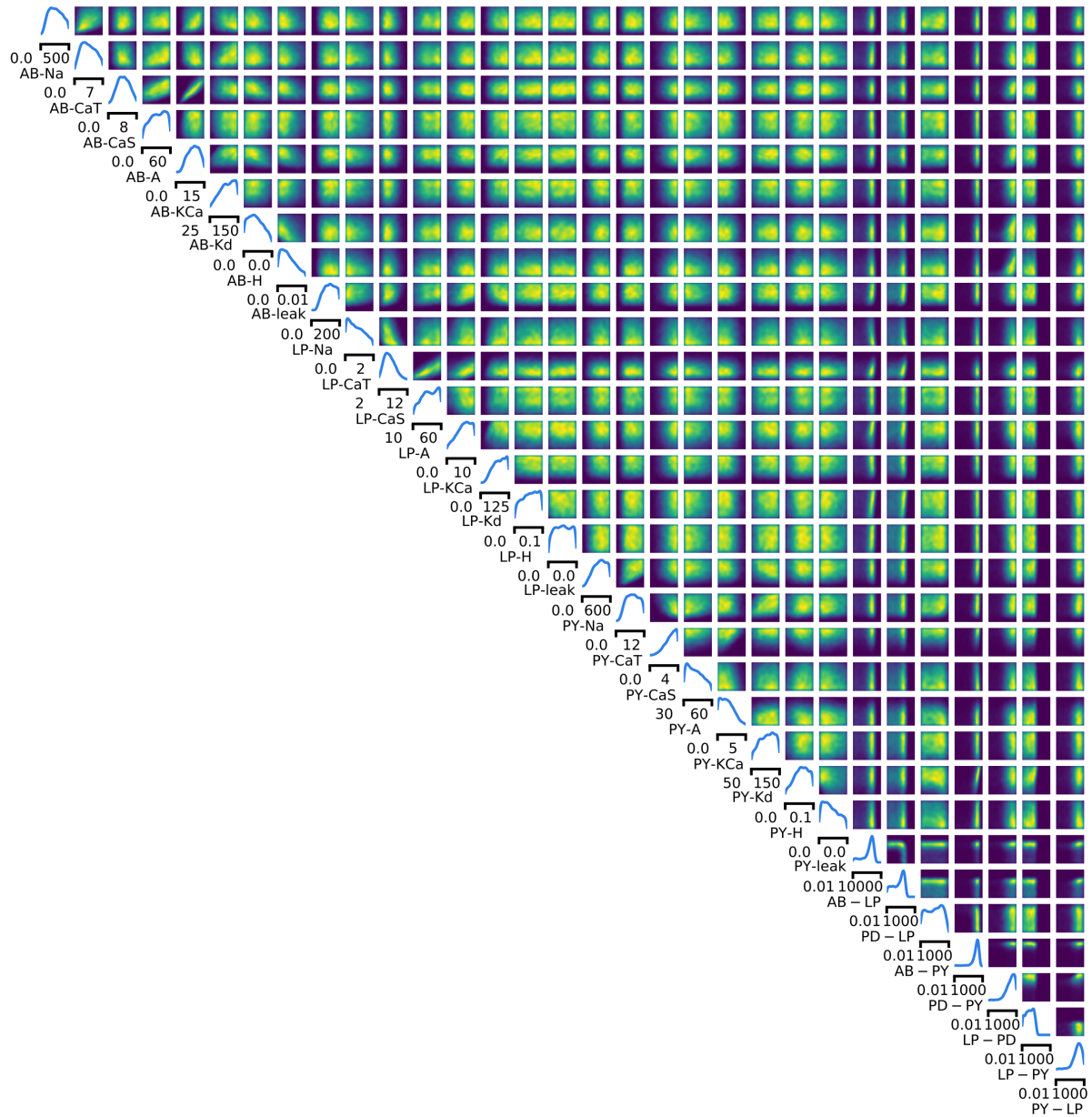
- 510 [4] A. A. Prinz, C. P. Billimoria, and E. Marder. Alternative to hand-tuning conductance-based models: construction and analysis of
511 databases of model neurons. *Journal of Neurophysiology*, 90(6):3998–4015, 2003.
- 512 [5] A. A. Prinz, D. Bucher, and E. Marder. Similar network activity from disparate circuit parameters. *Nature Neuroscience*, 7(12):
513 1345, 2004.
- 514 [6] G. M. Edelman and J. A. Gally. Degeneracy and complexity in biological systems. *Proceedings of the National Academy of Sciences*,
515 98(24):13763–13768, 2001.
- 516 [7] E. Marder and A. L. Taylor. Multiple models to capture the variability in biological neurons and networks. *Nature Neuroscience*,
517 14(2):133, 2011.
- 518 [8] J. N. MacLean, Y. Zhang, B. R. Johnson, and R. M. Harris-Warrick. Activity-independent homeostasis in rhythmically active
519 neurons. *Neuron*, 37(1):109–120, 2003.
- 520 [9] J. N. MacLean, Y. Zhang, M. L. Goeritz, R. Casey, R. Oliva, J. Guckenheimer, and R. M. Harris-Warrick. Activity-independent
521 coregulation of ia and ih in rhythmically active neurons. *Journal of Neurophysiology*, 94(5):3601–3617, 2005.
- 522 [10] R. N. Gutenkunst, J. J. Waterfall, F. P. Casey, K. S. Brown, C. R. Myers, and J. P. Sethna. Universally sloppy parameter sensitivities
523 in systems biology models. *PLoS Computational Biology*, 3(10):e189, 2007.
- 524 [11] R. Grashow, T. Brookings, and E. Marder. Compensation for variable intrinsic neuronal excitability by circuit-synaptic interac-
525 tions. *Journal of Neuroscience*, 30(27):9145–9156, 2010.
- 526 [12] T. O’Leary, A. C. Sutton, and E. Marder. Computational models in the age of large datasets. *Current Opinion in Neurobiology*, 32:
527 87–94, 2015.
- 528 [13] P. J. Gonçalves, J.-M. Lueckmann, M. Deistler, M. Nonnenmacher, K. Öcal, G. Bassetto, C. Chintaluri, W. F. Podlaski, S. A. Haddad,
529 T. P. Vogels, et al. Training deep neural density estimators to identify mechanistic models of neural dynamics. *Elife*, 9:e56261,
530 2020.
- 531 [14] A. Hasenstaub, S. Otte, E. Callaway, and T. J. Sejnowski. Metabolic cost as a unifying principle governing neuronal biophysics.
532 *Proceedings of the National Academy of Sciences*, 107(27):12329–12334, 2010.
- 533 [15] B. Sengupta, A. A. Faisal, S. B. Laughlin, and J. E. Niven. The effect of cell size and channel density on neuronal information
534 encoding and energy efficiency. *Journal of Cerebral Blood Flow & Metabolism*, 33(9):1465–1473, 2013.
- 535 [16] B. Sengupta and M. B. Stemmler. Power consumption during neuronal computation. *Proceedings of the IEEE*, 102(5):738–750,
536 2014.
- 537 [17] J. Astrup, P. M. Sørensen, and H. R. Sørensen. Oxygen and glucose consumption related to na⁺-k⁺ transport in canine brain.
538 *Stroke*, 12(6):726–730, 1981.
- 539 [18] J. Astrup, P. M. Sørensen, and H. R. Sørensen. Inhibition of cerebral oxygen and glucose consumption in the dog by hypothermia,
540 pentobarbital, and lidocaine. *Anesthesiology: The Journal of the American Society of Anesthesiologists*, 55(3):263–268, 1981.
- 541 [19] L. Sokoloff. Energetics of functional activation in neural tissues. *Neurochemical research*, 24(2):321–329, 1999.
- 542 [20] D. Attwell and S. B. Laughlin. An energy budget for signaling in the grey matter of the brain. *Journal of Cerebral Blood Flow &*
543 *Metabolism*, 21(10):1133–1145, 2001.
- 544 [21] H. Alle, A. Roth, and J. R. Geiger. Energy-efficient action potentials in hippocampal mossy fibers. *Science*, 325(5946):1405–1408,
545 2009.
- 546 [22] M. B. Stemmler, B. Sengupta, S. Laughlin, and J. Niven. Energetically optimal action potentials. In *Advances in neural information*
547 *processing systems*, pages 1566–1574, 2011.
- 548 [23] S. Onasch and J. Gjorgjieva. Circuit stability to perturbations reveals hidden variability in the balance of intrinsic and synaptic
549 conductances. *Journal of Neuroscience*, 40(16):3186–3202, 2020.
- 550 [24] B. C. Carter and B. P. Bean. Sodium entry during action potentials of mammalian neurons: incomplete inactivation and reduced
551 metabolic efficiency in fast-spiking neurons. *Neuron*, 64(6):898–909, 2009.
- 552 [25] B. Sengupta, M. Stemmler, S. B. Laughlin, and J. E. Niven. Action potential energy efficiency varies among neuron types in
553 vertebrates and invertebrates. *PLoS Comput Biol*, 6(7):e1000840, 2010.
- 554 [26] G. Yi, Y. Fan, and J. Wang. Metabolic cost of dendritic ca²⁺ action potentials in layer 5 pyramidal neurons. *Frontiers in neuro-*
555 *science*, 13, 2019.

- 556 [27] F. A. Roemschied, M. J. Eberhard, J.-H. Schleimer, B. Ronacher, and S. Schreiber. Cell-intrinsic mechanisms of temperature
557 compensation in a grasshopper sensory receptor neuron. *Elife*, 3:e02078, 2014.
- 558 [28] R. M. Harris-Warrick, E. Marder, A. I. Selverston, M. Moulins, T. J. Sejnowski, and T. A. Poggio. *Dynamic biological networks: the*
559 *stomatogastric nervous system*. MIT press, 1992.
- 560 [29] E. Marder and D. Bucher. Understanding circuit dynamics using the stomatogastric nervous system of lobsters and crabs. *Annu.*
561 *Rev. Physiol.*, 69:291–316, 2007.
- 562 [30] J.-M. Lueckmann, P. J. Goncalves, G. Bassetto, K. Öcal, M. Nonnenmacher, and J. H. Macke. Flexible statistical inference for
563 mechanistic models of neural dynamics. In *Advances in Neural Information Processing Systems*, pages 1289–1299, 2017.
- 564 [31] L. Stehlik, C. MacKenzie Jr, and W. Morse. Distribution and abundance of four brachyuran crabs on the northwest atlantic shelf.
565 *Fishery Bulletin*, 89(3):473–492, 1991.
- 566 [32] M. J. Donahue, A. Nichols, C. A. Santamaria, P. E. League-Pike, C. J. Krediet, K. O. Perez, and M. J. Shulman. Predation risk, prey
567 abundance, and the vertical distribution of three brachyuran crabs on gulf of maine shores. *Journal of Crustacean Biology*, 29
568 (4):523–531, 2009.
- 569 [33] C. J. Krediet and M. J. Donahue. Growth-mortality trade-offs along a depth gradient in cancer borealis. *Journal of Experimental*
570 *Marine Biology and Ecology*, 373(2):133–139, 2009.
- 571 [34] L. S. Tang, M. L. Goeritz, J. S. Caplan, A. L. Taylor, M. Fisek, and E. Marder. Precise temperature compensation of phase in a
572 rhythmic motor pattern. *PLoS Biol*, 8(8):e1000469, 2010.
- 573 [35] A. Moujahid, A. d’Anjou, F. Torrealdea, and F. Torrealdea. Energy and information in hodgkin-huxley neurons. *Physical Review*
574 *E*, 83(3):031912, 2011.
- 575 [36] L. M. Alonso and E. Marder. Visualization of currents in neural models with similar behavior and different conductance densities.
576 *eLife*, 8:e42722, 2019.
- 577 [37] S. A. Haddad and E. Marder. Recordings from the c. borealis stomatogastric nervous system at different temperatures in the
578 decentralized condition, July 2021. URL <https://doi.org/10.5281/zenodo.5139650>.
- 579 [38] S. A. Haddad and E. Marder. Circuit robustness to temperature perturbation is altered by neuromodulators. *Neuron*, 100(3):
580 609–623, 2018.
- 581 [39] J. S. Caplan, A. H. Williams, and E. Marder. Many parameter sets in a multicompartment model oscillator are robust to temper-
582 ature perturbations. *Journal of Neuroscience*, 34(14):4963–4975, 2014.
- 583 [40] L. M. Alonso and E. Marder. Temperature compensation in a small rhythmic circuit. *Elife*, 9:e55470, 2020.
- 584 [41] E. Marder. Variability, compensation, and modulation in neurons and circuits. *Proceedings of the National Academy of Sciences*,
585 108(Supplement 3):15542–15548, 2011.
- 586 [42] E. Marder, M. L. Goeritz, and A. G. Otopalik. Robust circuit rhythms in small circuits arise from variable circuit components and
587 mechanisms. *Current Opinion in Neurobiology*, 31:156–163, 2015.
- 588 [43] G. Papamakarios, T. Pavlakou, and I. Murray. Masked autoregressive flow for density estimation. In *Advances in Neural Infor-*
589 *mation Processing Systems*, pages 2338–2347, 2017.
- 590 [44] D. Greenberg, M. Nonnenmacher, and J. Macke. Automatic posterior transformation for likelihood-free inference. In *Interna-*
591 *tional Conference on Machine Learning*, pages 2404–2414, 2019.
- 592 [45] G. Le Masson, S. Przedborski, and L. Abbott. A computational model of motor neuron degeneration. *Neuron*, 83(4):975–988,
593 2014.
- 594 [46] W. B. Levy and R. A. Baxter. Energy-efficient neuronal computation via quantal synaptic failures. *Journal of Neuroscience*, 22
595 (11):4746–4755, 2002.
- 596 [47] B. Sengupta, M. B. Stemmler, and K. J. Friston. Information and efficiency in the nervous system—a synthesis. *PLoS Comput*
597 *Biol*, 9(7):e1003157, 2013.
- 598 [48] M.-J. Cabriol-Pol, D. Combes, V. S. Fénelon, J. Simmers, and P. Meyrand. Rare and spatially segregated release sites mediate a
599 synaptic interaction between two identified network neurons. *Journal of neurobiology*, 50(2):150–163, 2002.
- 600 [49] L. S. Tang, A. L. Taylor, A. Rinberg, and E. Marder. Robustness of a rhythmic circuit to short-and long-term temperature changes.
601 *Journal of Neuroscience*, 32(29):10075–10085, 2012.

- 602 [50] A. Rinberg, A. L. Taylor, and E. Marder. The effects of temperature on the stability of a neuronal oscillator. *PLoS Comput Biol*, 9
603 (1):e1002857, 2013.
- 604 [51] T. O’Leary and E. Marder. Temperature-robust neural function from activity-dependent ion channel regulation. *Current Biology*,
605 26(21):2935–2941, 2016.
- 606 [52] J. A. Haley, D. Hampton, and E. Marder. Two central pattern generators from the crab, *Cancer borealis*, respond robustly and
607 differentially to extreme extracellular pH. *Elife*, 7:e41877, 2018.
- 608 [53] S. Gorur-Shandilya, E. M. Cronin, A. C. Schneider, S. A. Haddad, P. Rosenbaum, D. Bucher, F. Nadim, and E. Marder. Mapping
609 circuit dynamics during function and dysfunction. *bioRxiv*, 2021.
- 610 [54] J. Ratliff, A. Franci, E. Marder, and T. O’Leary. Neuronal oscillator robustness to multiple global perturbations. *Biophysical
611 Journal*, 2021.
- 612 [55] G. Papamakarios and I. Murray. Fast ϵ -free inference of simulation models with bayesian conditional density estimation. In
613 *Advances in Neural Information Processing Systems*, pages 1028–1036, 2016.
- 614 [56] C. Durkan, I. Murray, and G. Papamakarios. On contrastive learning for likelihood-free inference. *International Conference on
615 Machine Learning*, 2020.
- 616 [57] L. Abbott and E. Marder. Modeling small networks, 1998.
- 617 [58] C. Durkan, A. Bekasov, I. Murray, and G. Papamakarios. Neural spline flows. In *Advances in Neural Information Processing Systems*,
618 pages 7511–7522, 2019.
- 619 [59] F. Pedregosa, G. Varoquaux, A. Gramfort, V. Michel, B. Thirion, O. Grisel, M. Blondel, P. Prettenhofer, R. Weiss, V. Dubourg,
620 J. Vanderplas, A. Passos, D. Cournapeau, M. Brucher, M. Perrot, and E. Duchesnay. Scikit-learn: Machine learning in Python.
621 *Journal of Machine Learning Research*, 12:2825–2830, 2011.
- 622 [60] K. He, X. Zhang, S. Ren, and J. Sun. Deep residual learning for image recognition. In *Proceedings of the IEEE conference on
623 computer vision and pattern recognition*, pages 770–778, 2016.
- 624 [61] N. Srivastava, G. Hinton, A. Krizhevsky, I. Sutskever, and R. Salakhutdinov. Dropout: a simple way to prevent neural networks
625 from overfitting. *The journal of machine learning research*, 15(1):1929–1958, 2014.
- 626 [62] P. G. Constantine. *Active subspaces: Emerging ideas for dimension reduction in parameter studies*. SIAM, 2015.
- 627 [63] R. M. Neal. Slice sampling. *The annals of statistics*, 31(3):705–767, 2003.

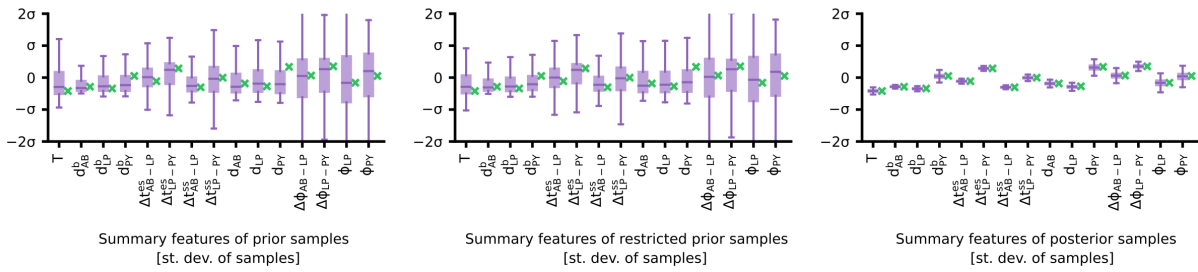
628 **Supplementary material**

629 **Supplementary figures**

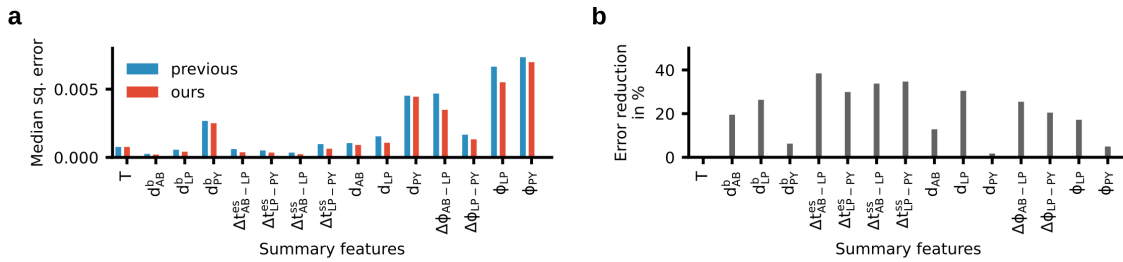


631 **Supplementary Figure 1. Full posterior distribution over circuit parameters given experimental data at 11°C.**

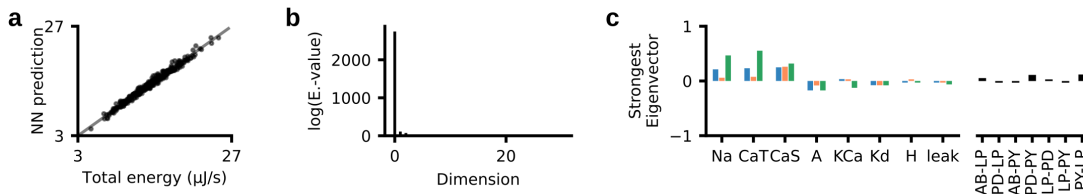
632 Panels on the diagonal are marginals, panels on the upper right are pairwise marginals. The first 24 parameters are
 633 membrane conductances, the last 7 parameters are synaptic conductances. All membrane conductances are maximal
 634 conductances and are given in mS/cm², all synaptic conductances are given in nS.



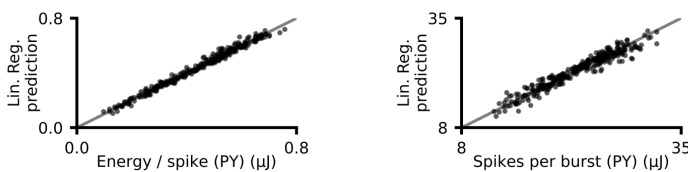
637 **Supplementary Figure 2. Summary features of activity produced by sampling from the prior, the restricted prior,**
 638 **and the posterior.** Experimentally observed activity in green. The boxplots indicate maximum, 75% quantile, median, 25%
 639 quantile, and minimum. All summary features are z-scored with the mean and standard deviation of all simulations from
 640 prior samples.



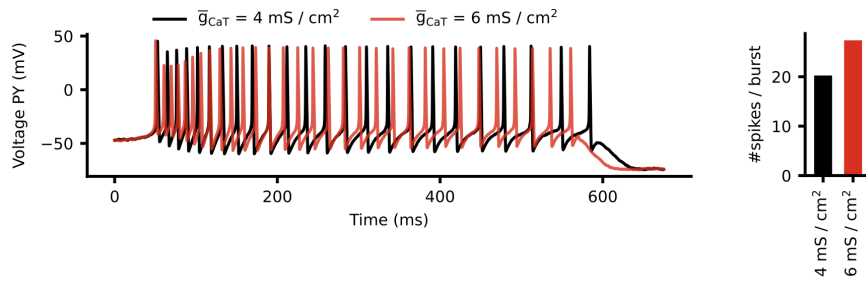
643 **Supplementary Figure 3. Accuracy of the enhanced version of SNPE versus accuracy in [13].** While we used half as
 644 many simulations (9 million versus 18 million), the accuracy of the method improved. (a) Median squared discrepancy
 645 between the experimentally measured activity and the activity produced by samples from the posterior. When using the
 646 classifier (red), the activity produced by posterior samples is closer to experimental activity than without the classifier
 647 (blue). (b) Reduction of mean squared discrepancy between our previous results and the presented method. All distances
 648 are computed after z-scoring the summary features with the mean and standard deviation of all prior samples.



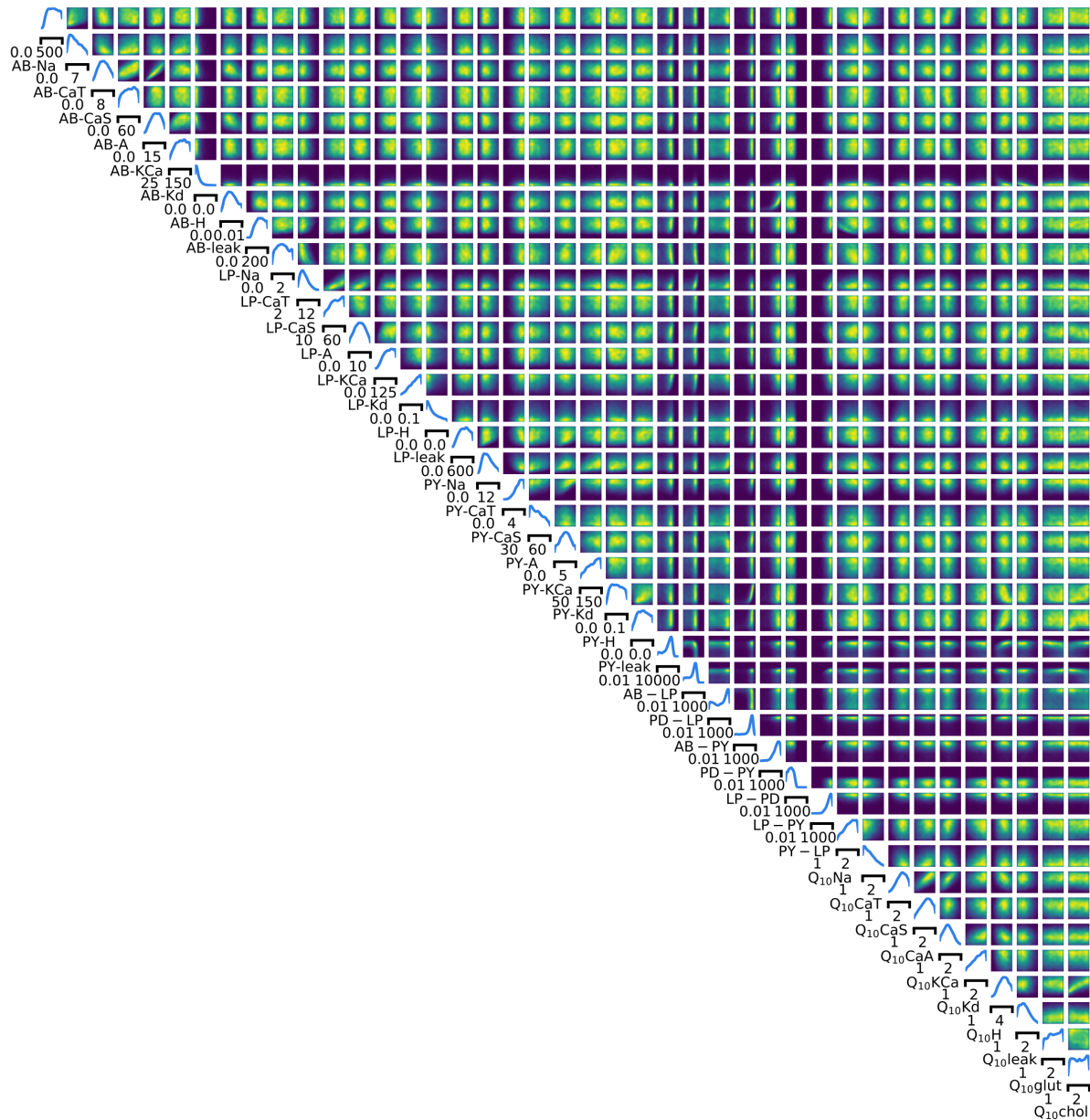
651 **Supplementary Figure 4. Neural network regression from circuit parameters onto the total energy consumption.**
 652 (a) Performance of a neural network predicting the total energy from circuit parameters. (b) Eigenvalue-spectrum of the
 653 trained neural network reveals a single dominating direction (details in Methods). (c) The eigenvector corresponding to the
 654 strongest eigenvalue is similar to the linear regression weights w (Fig. 4c).



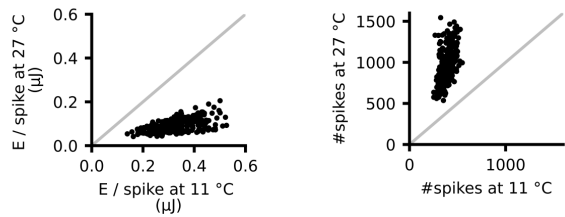
657 **Supplementary Figure 5. Performance of linear regression.** Left: Performance of linear regression from circuit
 658 parameters (taken from our database of 35,393 models) onto energy per spike in the PY neuron. Right: Performance of
 659 linear regression from circuit parameters onto the average number of spikes within a burst.



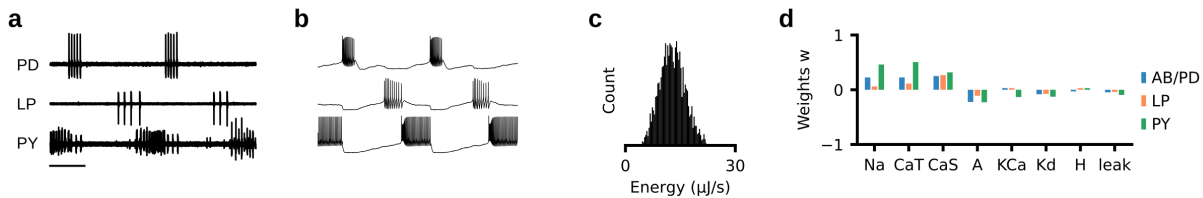
662 **Supplementary Figure 6. Influence of maximal conductance of transient calcium current on circuit function.** Left:
 663 Voltage trace in the PY neuron during activity produced by two circuit configurations (black and red) which are identical
 664 apart from the magnitude of \bar{g}_{CaT} . Right: The average number of spikes per burst in the PY neuron for the two
 665 configurations. The configuration with higher \bar{g}_{CaT} produces more spikes.



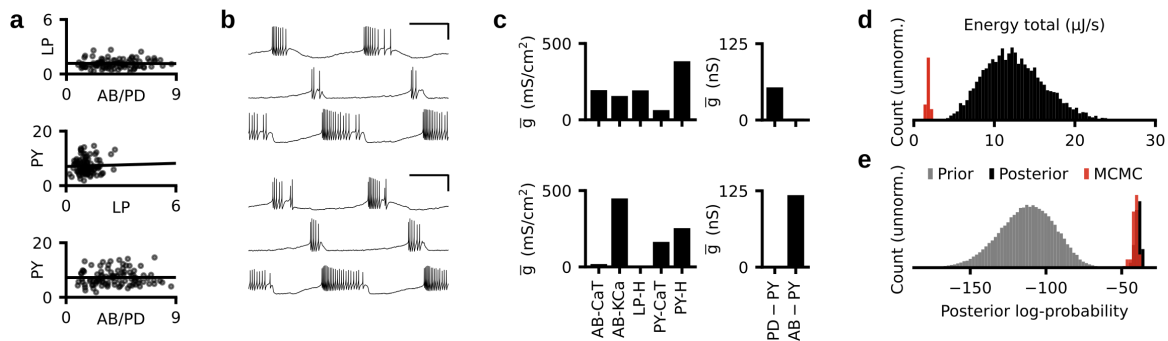
668 **Supplementary Figure 7. Full posterior distribution over 31 circuit parameters and 10 Q_{10} parameters given**
 669 **experimental data at 11°C and 27°C.**



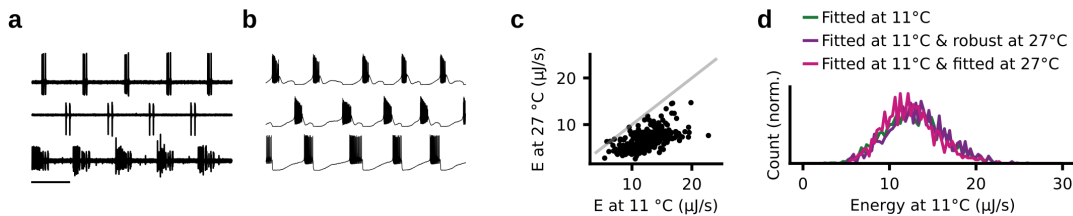
672 **Supplementary Figure 8. Energy consumption of the circuit at 11°C and at 27°C.** Energy per spike (left) and number of
 673 spikes (right) for parameter configurations simulated at 11°C and 27°C. The energy per spike is smaller at higher
 674 temperatures, but the number of spikes is higher at higher temperatures.



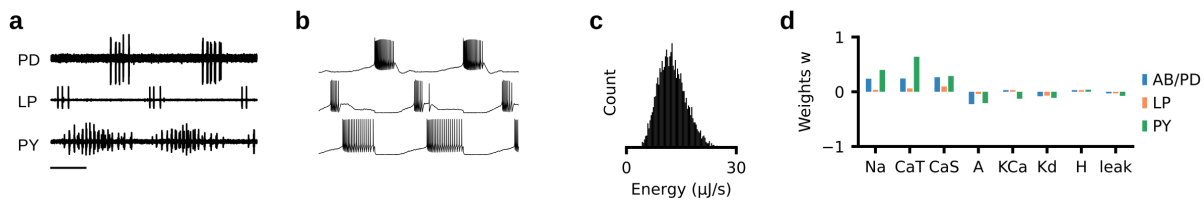
677 **Supplementary Figure 9. Analysis of a second experimental preparation.** (a) Experimental data recorded at 11°C. (b)
 678 Sample from posterior distribution matches the experimental data. (c) Energy consumption of 2804 model configurations
 679 that closely match experimental data. (d) Weights w of a linear regression from circuit parameters onto total energy
 680 consumption.



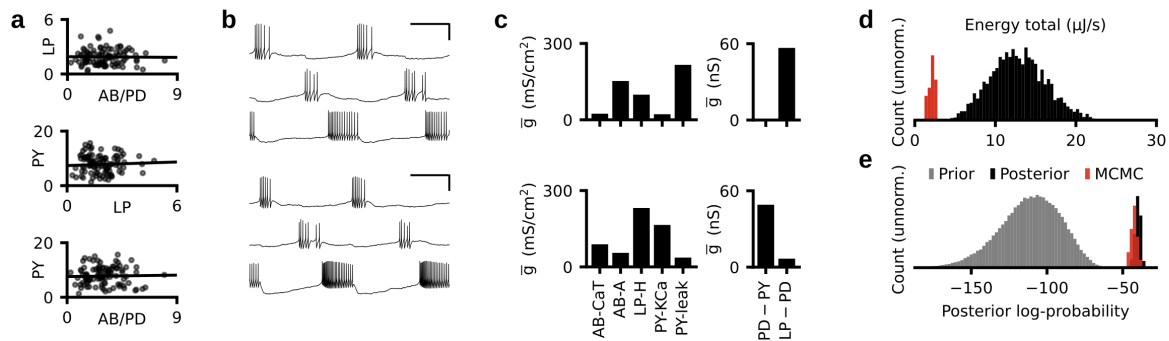
683 **Supplementary Figure 10. Tuning neurons individually, for a third experimental preparation.** (a) Black dots: Energy
 684 consumed by each neuron separately. Black line: Linear regression (correlation coefficient $r = -0.003$, p -value $p = 0.39$; LP
 685 versus PY, $r = 0.19$, $p = 0.007$; AB/PD versus PY, $r = 0.006$, $p = 0.77$). (b) The activity produced by two parameter
 686 configurations produced with the strategy described in Fig. 5b. (c) A subset of the membrane (left) and synaptic (right)
 687 conductances for the configurations in panel (c). The membrane conductances are scaled with the following factors (left to
 688 right): 100, 100, 10,000, 100, 10,000. (d) Histogram over the total energy consumption of all 6926 model configurations in
 689 our database and the energy consumption of the configurations produced with the strategy described in Fig. 5b (red). (e)
 690 Histogram of the posterior log-probability for samples from the prior distribution (grey), for the 6926 models in our
 691 database (black), and for the configurations produced with the strategy described in Fig. 5b (red).



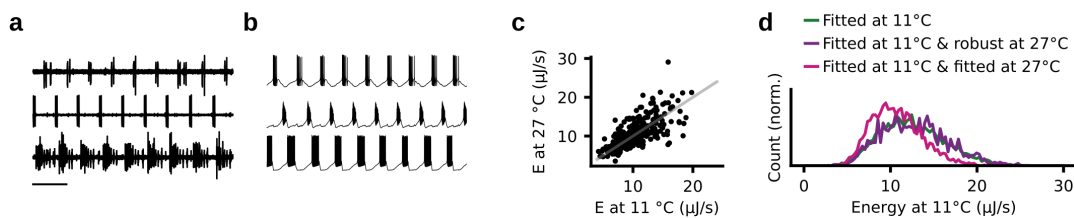
694 **Supplementary Figure 11. Analysis of temperature robustness of a second experimental preparation.** (a)
 695 Experimental data recorded at 27°C. (b) Sample from posterior distribution matches the experimental data. (c) Energy
 696 consumption at 11°C versus energy consumption at 27°C. (d) Green: Distribution of the energy consumption of circuits
 697 matching experimental data at 11°C. Purple: Distribution of the energy consumption of circuits that match data at 11°C
 698 and are robust at 27°C. Pink: Distribution of the energy consumption of circuits that match experimental data at 11°C and
 699 27°C.



702 **Supplementary Figure 12. Analysis of a third experimental preparation.** (a) Experimental data recorded at 11°C. (b)
 703 Sample from posterior distribution matches the experimental data. (c) Energy consumption of 6926 model configurations
 704 that closely match experimental data. (d) Weights w of a linear regression from circuit parameters onto total energy
 705 consumption.



708 **Supplementary Figure 13. Tuning neurons individually, for a second experimental preparation.** (a) Black dots:
 709 Energy consumed by each neuron separately. Black line: Linear regression (correlation coefficient $r = -0.009$, p-value
 710 $p = 0.39$; LP versus PY, $r = 0.21$, $p = 0.0012$; AB/PD versus PY, $r = 0.059$, $p = 0.10$). (b) The activity produced by two
 711 parameter configurations produced with the strategy described in Fig. 5b. (c) A subset of the membrane (left) and synaptic
 712 (right) conductances for the configurations in panel (c). The membrane conductances are scaled with the following factors
 713 (left to right): 100, 10, 10,000, 100, 10,000. (d) Histogram over the total energy consumption of all 2804 model
 714 configurations in our database and the energy consumption of the configurations produced with the strategy described in
 715 Fig. 5b (red). (e) Histogram of the posterior log-probability for samples from the prior distribution (grey), for the 2804
 716 models in our database (black), and for the configurations produced with the strategy described in Fig. 5b (red).



719 **Supplementary Figure 14. Analysis of temperature robustness of a third experimental preparation.** (a)
 720 Experimental data recorded at 27°C. (b) Sample from posterior distribution matches the experimental data. (c) Energy
 721 consumption at 11°C versus energy consumption at 27°C. (d) Green: Distribution of the energy consumption of circuits
 722 matching experimental data at 11°C. Purple: Distribution of the energy consumption of circuits that match data at 11°C
 723 and are robust at 27°C. Pink: Distribution of the energy consumption of circuits that match experimental data at 11°C and
 724 27°C.